OXFORD

Journal of Petrology, 2023, **64**, 1–27
https://doi.org/10.1093/petrology/egad051
Advance access publication date 3 July 2023
Original Manuscript

Into the High to Ultrahigh Temperature Melting of Earth's Crust: Investigation of Melt and Fluid Inclusions within Mg-Rich Metapelitic Granulites from the Mather Peninsula, East Antarctica

Zhao Liu[1], Bruna B. Carvalho[2], Wancai Li[3], Laixi Tong[1,*], Omar Bartoli[2], Longyao Chen[4], Qinghe Yan[5] and Haobo Wu[1]

[1]State Key Laboratory of Continental Dynamics, Department of Geology, Northwest University, Xi'an 710069, China
[2]Dipartimento di Geoscienze, Università di Padova, Via Gradenigo 6, Padua 35131, Italy
[3]CAS Key Laboratory of Crust–Mantle Materials and Environments, School of Earth and Space Sciences, University of Science and Technology of China, Hefei 230026, China
[4]Key Laboratory of Paleomagnetism and Tectonic Reconstruction of Ministry of Natural Resources, Institute of Geomechanics, Chinese Academy of Geological Sciences, Beijing 100081, China
[5]School of Resource Environment and Earth Science, Yunnan University, Kunming 650091, China

*Corresponding author. Telephone: +86 029-88302312. E-mail: tonglx@nwu.edu.cn

Abstract

Precise constraints on the compositions of melts generated by anatexis under ultrahigh temperature (*UHT*) conditions are critical for understanding processes of partial melting and differentiation of the Earth's crust. Here we reveal geochemical and physical signatures of anatectic melts preserved as nanogranitoids (i.e. crystalized melt inclusions) within sapphirine-bearing *UHT* metapelitic granulites from the Mather Peninsula, East Antarctica. Their coexistence with high−Al orthopyroxene as inclusions in garnets strongly suggests that the investigated melts were at least partially *UHT* in origin. The nanogranitoids are enriched in SiO_2 (69.9–75.6 wt.%), strongly peraluminous (ASI values = 1.2–1.6) and potassic to ultrapotassic ($Na_2O + K_2O$ = 7.1–9.5 wt.%, K/Na = 2.2–9.3). When compared to the granulitic restite, the melts are enriched in Li, Cs, Rb, Ta, Sm, Nd, Zr, U and Pb, and depleted in Ce, Th, Ba, Sr and Nb. Their geochemical characteristics are consistent with biotite−dehydration melting in the absence of plagioclase. Our calculation results indicate that these hot crustal melts have low densities of 2.47 ± 0.07 g/cm^3, low viscosities of $10^{4.9 \pm 1.2}$ Pa·s and high heat production values of ~2.8 μW/m^3. Therefore, such melts are mobile and susceptible to be extracted from the source, and consequently their flow and removal from the deep crust may greatly affect the chemical and thermal structure of the continental crust.

Secondary C − O − H fluid inclusions within garnet and orthopyroxene have also been detected. These inclusions contain magnesite, pyrophyllite, corundum, with or without residual CO_2. The minerals within the fluid inclusions are interpreted as stepdaughter minerals, which were produced by the reaction of the fluid with its host. The metamorphic timing of the investigated rocks is still a matter of debate. Zircon U–Pb dating results obtained in this study suggest that the metapelitic granulites may have undergone two separated thermal events at ~1000 and ~530 Ma, respectively. The presence of fluid inclusions indicates that fluid infiltration and Pan–African reworking may have played an important role in obscuring chronological information of the early thermal scenario in poly-metamorphic terranes.

Key words: East Antarctica; Mather Peninsula; C–O–H fluid; Melt inclusions; UHT metamorphism

INTRODUCTION

Ultrahigh temperature (*UHT*) metamorphism is the most thermally extreme type of crustal metamorphism, with peak temperatures exceeding 900°C at moderate pressures (7–13 kbar) (Harley, 1998a, 2008), with *dT/dP* values of 66–200°C/kbar (Harley, 2021). *UHT* metamorphism is now recognized as a relatively common rather than anomalous process of the Earth's crust due to (1) its wide age distribution ranging from Archean to Quaternary (e.g. Brown, 2007; Pownall *et al.*, 2014; Harley, 2021; Zhang *et al.*, 2022); and (2) its extensive exposures around the world (>70 localities; Harley, 2021; Lei & Xu, 2018) related to various geodynamic processes. For example, *UHT* metamorphism may occur in tectonic backgrounds associated with (1) lithospheric extension and underplating of mantle-derived magmas as a result of slab rollback (e.g. Pownall *et al.*, 2014), mantle plume activity (e.g. Tong *et al.*, 2014a; Liu *et al.*, 2020); (2) oceanic ridge subduction (e.g. Santosh *et al.*, 2012), and inversion and thickening of hot back-arc (e.g. Brown, 2007); (3) long-lived orogenic self-heating by radioactive elements (e.g. Clark *et al.*, 2011; Zhang *et al.*, 2022); or (4) a combined contribution from several driving forces (Huang *et al.*, 2019, 2021).

High temperature (*HT*) to *UHT* metamorphism of crustal rocks inevitably produces anatectic melts at depth, and their loss yields a refractory lower crust, whereas ascent and emplacement of granitic melts at shallower levels create a more silicic upper crust (e.g. Brown, 2007, 2013; Sawyer *et al.*, 2011). Furthermore,

Received: August 1, 2022. **Revised:** June 28, 2023. **Accepted:** June 29, 2023

it may result in decrease of the rock strength and variations in bulk compositions of the granulitic rocks (e.g. Rosenberg & Handy, 2005; Diener & Fagereng, 2014; Cavalcante *et al.*, 2016). However, interpretations of melting mechanisms of crustal rocks remain a long-standing challenge, which have been traditionally tracked with the aid of (1) geochemistry of granites and leucosomes (e.g. Zeng *et al.*, 2005; Gao *et al.*, 2017; Wolf *et al.*, 2019), (2) phase equilibria modeling at specific *P–T* conditions (e.g. White *et al.*, 2004, 2014; Wei, 2016; Huang *et al.*, 2021), and (3) melting experiments on natural rocks under variable *P–T–*X_{H2O} conditions (refer to Gao *et al.*, 2016 and references therein). Furthermore, a recent progress is to conduct in situ observations and analyses on nanogranitoid inclusions (partially to totally crystallized melt inclusions preserved in peritectic phases; named after Cesare *et al.*, 2015) and their glassy counterparts (e.g. Cesare *et al.*, 2009, 2015; Acosta Vigil *et al.*, 2010, 2012; Ferrero *et al.*, 2012, 2016, 2018, 2021a, 2021b; Bartoli *et al.*, 2013a, 2013b, 2014, 2016, 2019; Gao *et al.*, 2014; Borghini *et al.*, 2018, 2023; Ferrero & Angel, 2018; Carvalho *et al.*, 2019, 2023a; Ferri *et al.*, 2020; Bartoli & Carvalho, 2021; Gianola *et al.*, 2021; Tacchetto *et al.*, 2021; Higashino & Kawakami, 2022). Thus far, melt inclusions have been only recognized in a few *UHT* metapelitic terranes, including (1) the Ivrea Zone (NW Italy) (Carvalho *et al.*, 2019), (2) the Kerala Khondalite Belt (India) (Cesare *et al.*, 2009; Ferrero *et al.*, 2012), (3) the Gruf Complex (European Central Alps) (Gianola *et al.*, 2021), (4) the Lützow–Holm Complex (East Antarctica) (Kawakami & Motoyoshi, 2004; Hiroi *et al.*, 2019; Suzuki & Kawakami, 2019; Carvalho *et al.*, 2023a), (5) the Sør Rondane Mountains (East Antarctica) (Higashino & Kawakami, 2022), and (6) the Chinese Altai orogen (NW China) (Liu *et al.*, 2020). It is worth noting that the occurrence of nanogranitoids in *UHT* rocks does not imply automatically that they reflect the *UHT* crustal melts because melts can be trapped during the *HT* prograde metamorphism (refer to Gianola *et al.*, 2021). A better understanding of potential effects of *UHT* metamorphism on the differentiation and dynamic evolution of the crust demands that the hottest crustal melts are chemically characterized, in particular for their major and trace elements.

The Mather metapelitic granulites from the Rauer Islands (East Antarctica) are a world-renowned poly-metamorphic *UHT* lithology, with peak *P–T* conditions of 8.5–12 kbar and 950–1050°C (Harley & Fitzsimons, 1991; Harley, 1998b, 2016; Tong & Wilson, 2006; Kelsey *et al.*, 2007; Harley *et al.*, 2009; Clark *et al.*, 2019; Chen *et al.*, 2023). In this contribution, we conduct an integrated investigation of microstructural features, major and trace element contents of nanogranitoid inclusions (NIs) preserved within garnet porphyroblasts. Data collected in this work are fundamental to the understanding of melting regimes of crustal rocks under *UHT* conditions, and their contribution to crustal differentiation and orogenic evolution. Secondary fluid inclusions (FIs) in peritectic phases are also characterized to reveal the nature of post–peak infiltrated fluid, and to evaluate its potential role in resetting the U–Pb clock of zircons.

GEOLOGICAL SETTING

The Antarctic continent is separated by the Transantarctic Mountains into two distinct geological units, namely East Antarctica and West Antarctica. East Antarctica is one of the largest cratons around the world, documenting more than 3.5 billion years of evolutional history (Harley *et al.*, 2013). The Prydz Belt was recognized as a tectonic mobile belt in East Antarctica that has been extensively affected by the Pan–African (~530 Ma) thermal event (e.g. Hensen & Zhou, 1997; Harley *et al.*, 1998; Kelsey *et al.*, 2003, 2007; Harley & Kelly, 2007; Wang *et al.*, 2007, 2008, 2022; Liu *et al.*, 2009, 2021; Grew *et al.*, 2012; Tong *et al.*, 2014b, 2019). The tectonic nature of the Prydz Belt remains debated and there are two main schools of thought; one considers that it represents a Pan–African suture zone associated with the final assembly of East Gondwana (e.g. Zhao *et al.*, 1995; Hensen & Zhou, 1997; Fitzsimons, 2003; Kelsey *et al.*, 2007; Liu *et al.*, 2021; Wang *et al.*, 2022), and the other views it as a Pan–African intraplate orogen related to intracontinental reworking (e.g. Phillips *et al.*, 2007; Wilson *et al.*, 2007; Tong *et al.*, 2014b, 2019; Ren *et al.*, 2016).

The Rauer Islands are located on the eastern margin of the Prydz Belt, with the Brattstrand Bluff and Larsemann Hills to the southwest, and the Vestfold Hills to the northeast. The Rauer Islands were thought to be texturally correlated with the Rengali–Eastern Chats Province, forming parts of the Indo–Antarctica supercontinent (e.g. Sawant *et al.*, 2017). Archean and Proterozoic crustal components have been recognized from the Rauer Islands (Kinny *et al.*, 1993). The Proterozoic domain comprises metamorphosed 1420–1000 Ma mafic–intermediate–felsic intrusive rocks (Kinny *et al.*, 1993; Liu *et al.*, 2021). The early Neoproterozoic (i.e. Grenville aged; 1000–900 Ma) and late Neoproterozoic/Cambrian (i.e. Pan–African aged; 590–500 Ma) ages have been identified from metamorphic rocks in this region (e.g. Kinny *et al.*, 1993; Kelsey *et al.*, 2007; Liu *et al.*, 2021). The Archean domain predominantly consists of tonalitic to granitic orthogneisses with three age clusters of 3470–3270, 2840–2800 and ~2550 Ma (Kinny *et al.*, 1993; Harley *et al.*, 1998; Hokada *et al.*, 2016; Liu *et al.*, 2021). This domain also contains Fe- or Mg-rich layered mafic complexes that were subjected to a granulite facies metamorphism in the Cambrian (Harley *et al.*, 1998; Harley & Kelly, 2007; Chen *et al.*, 2023). Although Pan–African ages have been widely recognized in the Archean domain (e.g. Kelsey *et al.*, 2003, 2007; Wang *et al.*, 2007; Hokada *et al.*, 2016; Clark *et al.*, 2019; Liu *et al.*, 2021), it is still unclear whether it was also involved in the Grenville–aged tectono-thermal event.

The Rauer Islands consist of two paragneiss successions, namely the Filla and the Mather Paragneisses (Fig. 1a; Harley & Fitzsimons, 1991). These two paragneiss successions are mainly distributed on the Proterozoic and Archean crustal domains, respectively. Deposition ages of the Filla Paragneiss have been constrained to be Mesoproterozoic (Sims *et al.*, 1994; Liu *et al.*, 2021). This unit was considered to have experienced a prominent metamorphic event at 1030–970 Ma and a high-grade reworking at 575–510 Ma (e.g. Kinny *et al.*, 1993; Kelsey *et al.*, 2007; Liu *et al.*, 2021). The Mather Paragneiss typically comprises magnesian and aluminous garnet–orthopyroxene–sillimanite-bearing metapelite, orthopyroxene–sillimanite metaquarzite, magnesian garnet–orthopyroxene metapelite and garnet-bearing mafic granulite (Fig. 1b; Harley *et al.*, 1995; Harley, 1998b). This suite usually occurs as thin and laterally discontinuous horizons from the Mather Peninsula to the Short Point in the eastern Rauer Islands (Hokada *et al.*, 2016). Mather Paragneiss preserves strong evidence for *UHT* metamorphism, with exposures of sapphirine-bearing metapelitic granulites on the Mather Peninsula (e.g. Harley, 1998b; Tong & Wilson, 2006) and the Torckler Island (Harley *et al.*, 2009), with peak *P–T* conditions of 8.5–12 kbar and 1000–1050°C (e.g. Harley, 1998b, 2016; Tong & Wilson, 2006). The sapphirine–bearing *UHT* gneisses preserve inherited zircon ages of 2800–2400 Ma (e.g. Wang *et al.*, 2007; Hokada *et al.*, 2016), and are hosted by ~3267 Ma tonalitic orthogneisses (Hokada *et al.*, 2016). However, timing of the *UHT* metamorphism is still a matter of debate.

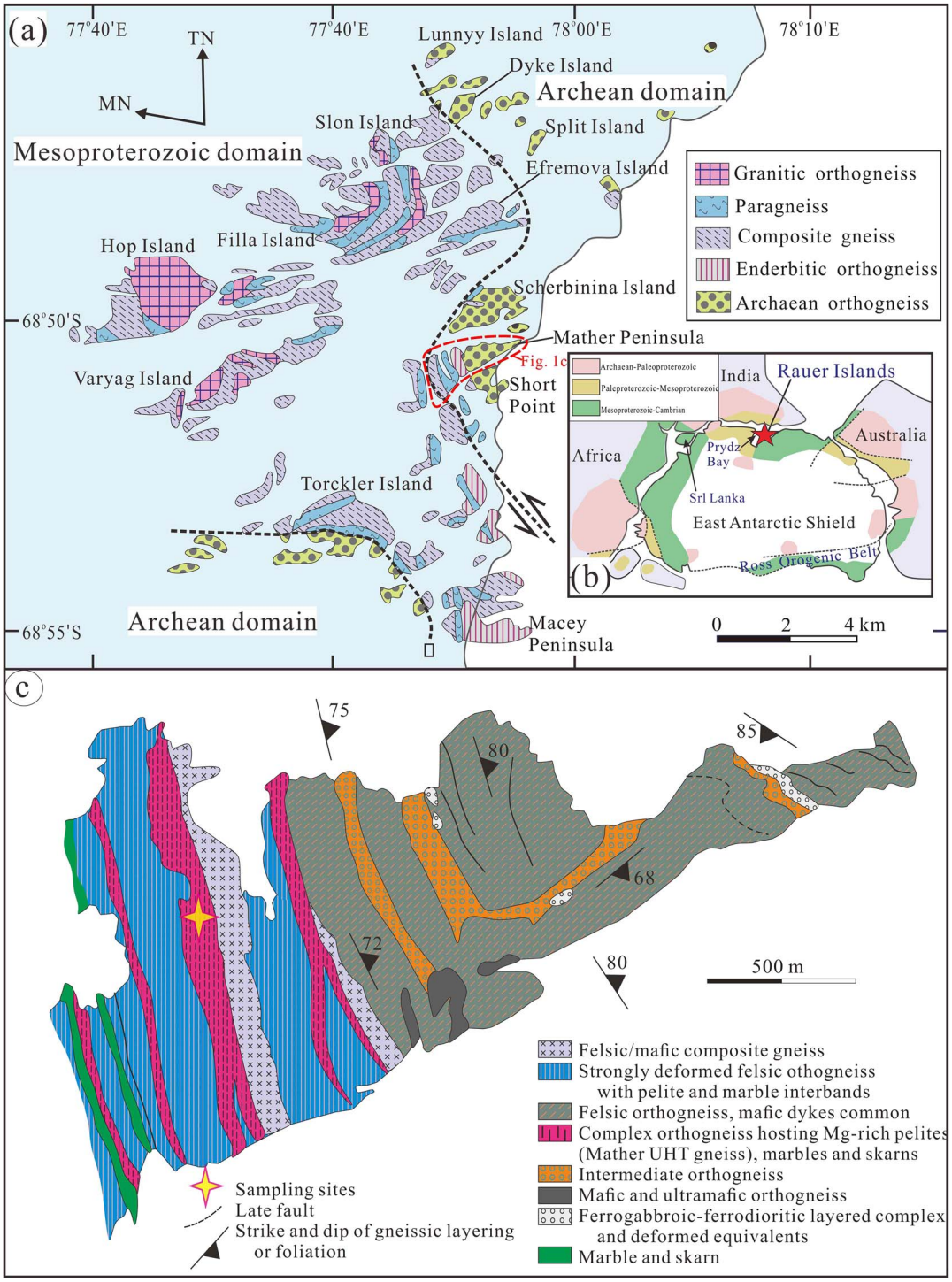

Fig. 1. (a) Simplified geological map of the Rauer Islands, East Antarctica (after Harley & Fitzsimons, 1991; Tong & Wilson, 2006; Tong *et al.*, 2021). The black dashed line represents the boundary between Mesoproterozoic and Archean crustal components. (b) Location of the Rauer Islands in the reconstructed Gondwana supercontinent at ~500 Ma (modified after Fitzsimons, 2000; Wilson *et al.*, 2007; Hokada *et al.*, 2016). (c) Lithological distribution and sample locality on the Mather Peninsula (after Harley, 1998b; Hokada *et al.*, 2016).

Some researchers argued that the *UHT* metamorphism occurred at ~1000 Ma and the subsequent decompression and final cooling happened at ~530 Ma (e.g. Tong & Wilson, 2006; Wang *et al.*, 2007) while others considered that the *UHT* metamorphism occurred in the Cambrian (e.g. Kelsey *et al.*, 2003, 2007; Clark *et al.*, 2019) or prior to 590–580 Ma (Harley *et al.*, 2009; Hokada *et al.*, 2016).

PETROGRAPHY

The granulite sample RG16–80 (68°50'50" S and 77°54'43" E) was collected from the Mather Peninsula in the Rauer Islands, East Antarctica (Fig. 1b). Compositions and mineral assemblages vary considerably at outcrop scale, ranging from quartz-bearing to SiO_2-undersaturated rocks (refer to Harley, 1998b for more details). The studied rocks occur as discrete rafts or

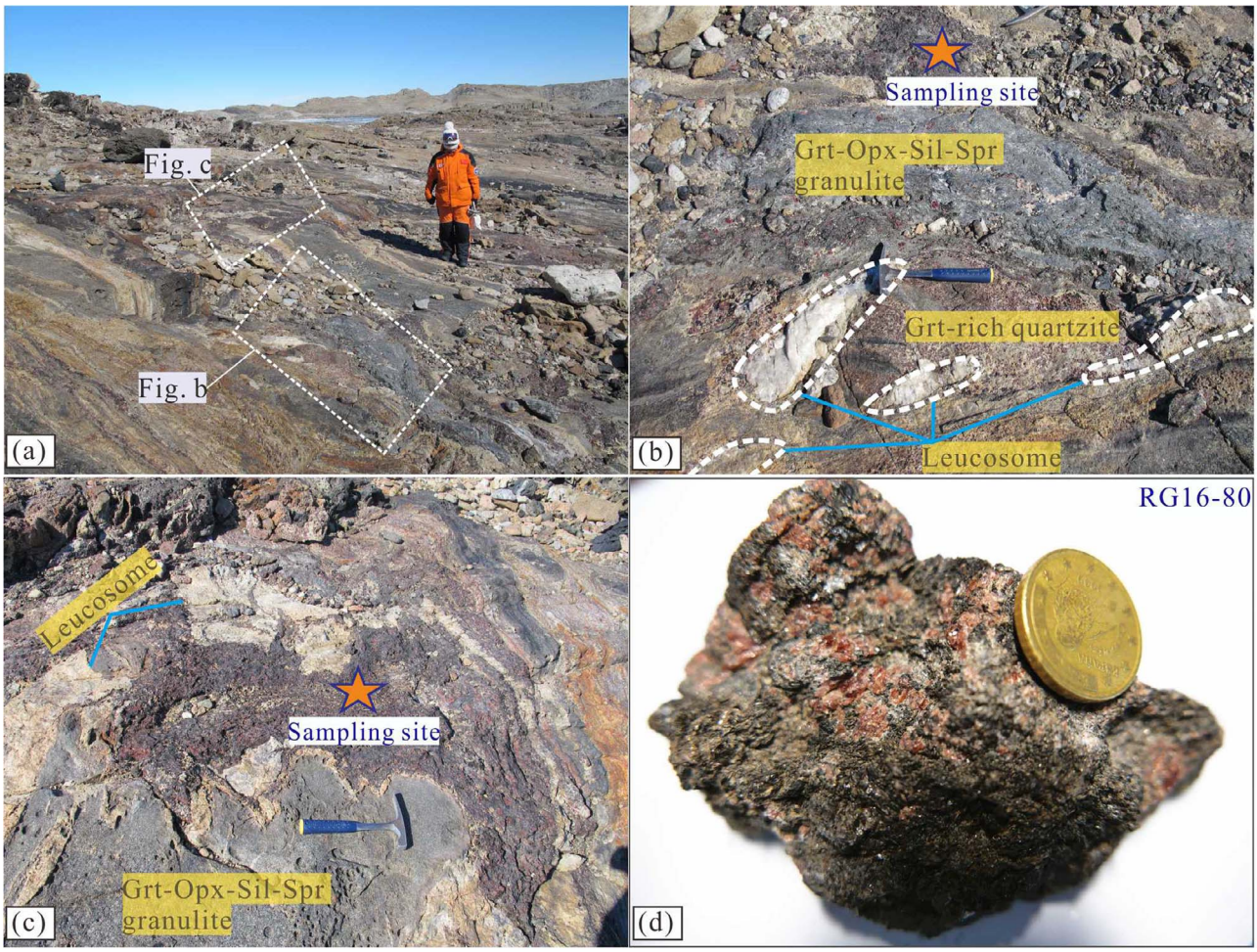

Fig. 2. (a) A Field photograph showing the occurrence of *UHT* granulites from the Mather Peninsula, East Antarctica. (b,c) Enlarged photographs of white boxes in (a) displaying the presence of different lithological components. The sampling sites are shown by orange stars. The hammer for scale is 25 cm in length. (d) A representative hand specimen of the studied rocks. The coin for scale is about 2.4 cm in diameter.

boudins interlayering with Grt–Opx–Sil–Spr granulites, Grt-rich quartzites, Grt–Sil metapelites, two-pyroxene granulites, Opx–Sil–(Per)- bearing and Spr–Opx–Kfs-bearing leucogneisses (Fig. 2). Mineral abbreviations are from Warr (2021). The studied Mg-rich metapelites constitute 5–8% of the outcrop, and are roughly parallel to foliation S6 (Tong & Wilson, 2006), corresponding to the composite high–strain fabric described by Dirks & Wilson (1995). The samples are coarse–grained, with an assemblage of orthopyroxene (35–45%), biotite (25–30%), garnet (~15%), cordierite (7–10%), minor sapphirine, plagioclase, K-feldspar, quartz (<5%), and accessory spinel, ilmenite, apatite, zircon and monazite (Fig. 3).

Garnet porphyroblasts are subhedral to anhedral, with sizes varying from 0.1 to 30 mm. They usually preserve corroded biotite and quartz inclusions in cores. Most orthopyroxene grains are present as porphyroblasts (up to 1.2 cm in diameter), and in rare cases, they may contain platy or rounded biotite inclusions (Fig. 3a, b). The inclusions within garnet cores and orthopyroxene, such as biotite and quartz, are considered as pre-peak (M0) minerals. The cores of orthopyroxene porphyroblasts are considered to have been formed at M0 stage because they contain relatively low Al_2O_3 contents (<6.5 wt.%) compared with the rim (>8.0 wt.%; Opx_1) (see details on the section of mineral chemistry), and high Al_2O_3 contents in orthopyroxene usually suggest that they were formed under *UHT* conditions (e.g. Harley, 1998a).

Sometimes, orthopyroxene with high Al_2O_3 contents (up to 8.85–9.04 wt.%) may occur as inclusions within garnet mantle (Fig. 3a), and both minerals are considered to form at, or close to, peak conditions. Collectively, garnet mantles, orthopyroxene rims, high–Al orthopyroxene inclusions within garnets and biotite porphyroblasts (Fig. 3b) are interpreted to be formed at the metamorphic peak (M1) stage. K-feldspar occurs in very local domains, and is usually 0.5–4.0 mm in size (Fig. 3c). However, it is difficult to determine whether K-feldspar was formed at M0 or M1 stage based on petrographic observations.

The presence of biotite and quartz inclusions within garnets, coupled with the formation of garnet and orthopyroxene porphyroblasts, implies the progress of the following Bt – dehydration melting reaction:

$$Bt\ (+\ Kfs) + Qz \rightarrow Grt + Opx + melt.$$

Garnet porphyroblasts are commonly replaced at their margins by the intergrowth of orthopyroxene (Opx_2) + cordierite ± biotite ± plagioclase ± spinel (Fig. 3d, e), which are assigned to the post-peak (M2) assemblage. Formation of the intergrowth is considered to result from the following decompression-related reaction:

$$Grt \rightarrow Opx_2 + Crd \pm Spl$$ (e.g. Harley, 1998b; Santosh *et al.*, 2012).

Intergrowths of sapphirine + cordierite are found in the matrix (Fig. 3f). Occasionally, vermicular low-Al orthopyroxene and

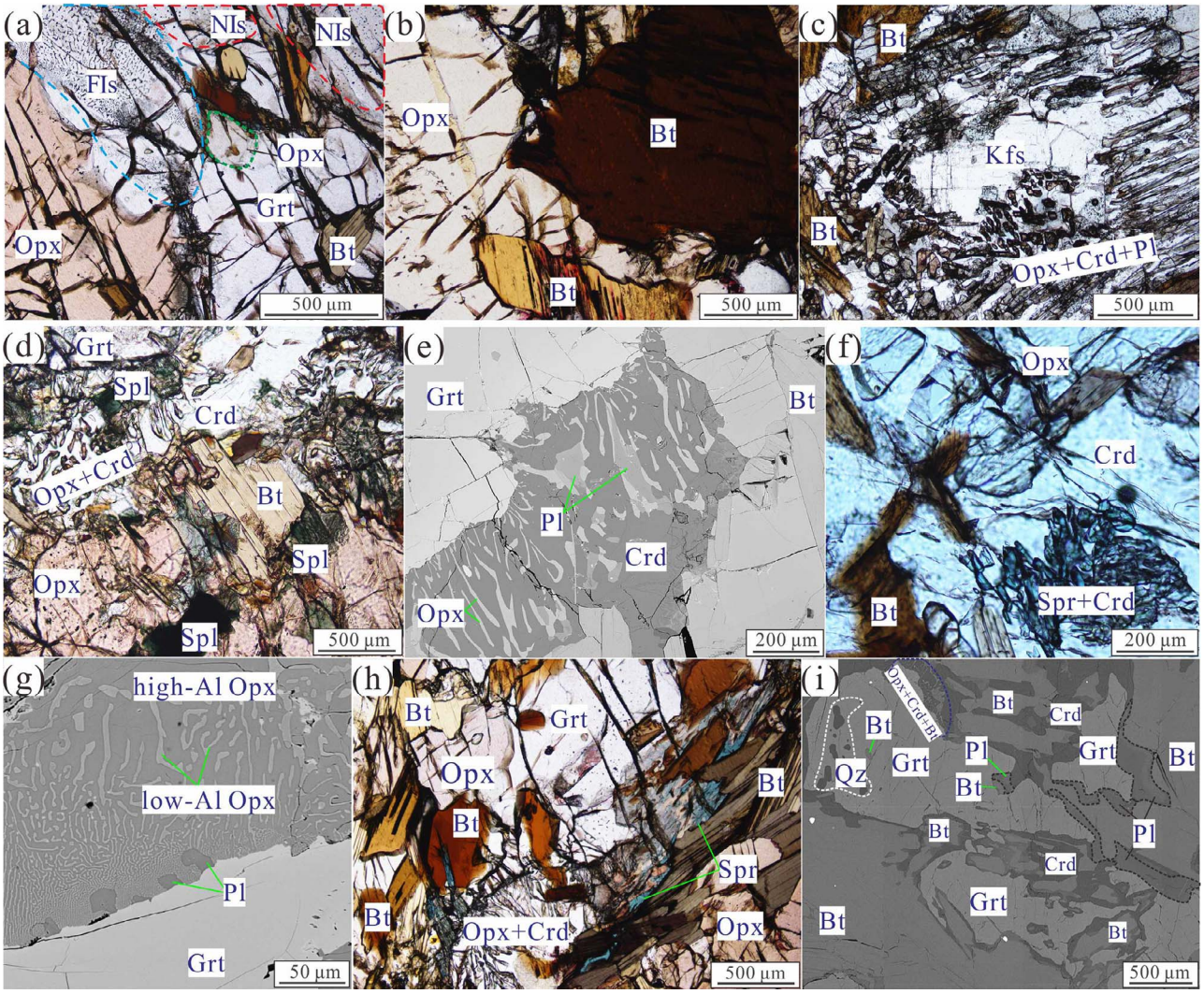

Fig. 3. Plane polarized light photomicrographs and BSE images of the Mather *UHT* granulite sample RG16–80. (a) Co-existence of garnet and orthopyroxene porphyroblasts. High-Al orthopyroxene inclusion within garnet is outlined by green dashed lines in the figure, which coexists with primary NIs (outlined by red dashed lines). Also shown in this figure are secondary FIs, highlighted with blue dashed lines. (b) Coexistence of biotite and orthopyroxene porphyroblasts, with a biotite inclusion within orthopyroxene. (c) K-feldspar grain rimmed by the intergrowth of orthopyroxene + cordierite + plagioclase. (d) Garnet and orthopyroxene porphyroblasts separated by fine-grained intergrowths of orthopyroxene + cordierite. (e) A BSE image showing the intergrowth of orthopyroxene + cordierite + plagioclase around garnets. (f) Intergrowths of sapphirine + cordierite in the matrix. (g) BSE image showing vermicular low-Al orthopyroxene in the rim of a high-Al orthopyroxene porphyroblast. (h) Biotite + plagioclase symplectites surrounding orthopyroxene. (i) Elongated garnet, cordierite, biotite, plagioclase in strongly deformed domains. Interstitial plagioclase is outlined by dashed black lines while quartz inclusions within garnets are highlighted with white dashed lines.

plagioclase are preserved in the rim of high-Al orthopyroxene porphyroblasts (Fig. 3g). These microstructures are also interpreted to form at the post–peak (M2) stage.

Some medium- to fine-grained sapphirine strips are associated with oriented biotite, which sometimes, may surround orthopyroxene + cordierite intergrowths (Fig. 3h). In strongly deformed domains, elongated garnet, cordierite, biotite, plagioclase, rare orthopyroxene and spinel grains show a similar orientation (Fig. 3i), which may have been formed at the final cooling (M3) stage. The appearance of interstitial plagioclase films suggests the presence of former melts (Fig. 3i) (e.g. Holness *et al.*, 2011).

The presence of retrograde biotite and plagioclase is in agreement with progress of the following reaction:

$$\text{Grt (Opx)} + \text{melt} \rightarrow \text{Bt} + \text{Pl} \pm \text{Qz}.$$

In summary, the Spr-bearing *UHT* granulites (sample RG16–80) from the Mather Peninsula preserve four–stage metamorphic assemblages: (1) M0 stage is represented by the Bt–Qz-bearing inclusions and the cores of garnet and orthopyroxene porphyroblasts; (2) M1 stage is marked by the growth of garnet–orthopyroxene$_1$–biotite in the presence of melt, with or without the presence of K – feldspar; (3) M2 stage is featured by the development of orthopyroxene$_2$ + cordierite ± biotitet ± plagioclase ± spinel and sapphirine + cordierite intergrowths surrounding the peak garnet or orthopyroxene; and (4) M3 stage is characterized by the growth of cordierite–biotite–plagioclase-bearing assemblages during the crystallization of melts.

ANALYTICAL METHODS

Back-scattered electron imaging, X-ray mapping and EPMA analysis

Analyses of major elements in minerals and back-scattered electron (BSE) imaging were conducted using JEOL JXA–8230 electron

probe microanalyzer (EPMA) at the Department of Geology, Northwest University, Xi'an, China. Additional X-ray mapping of NIs was done using JEOL JXA–8230 EPMA at the Wuhan Sample Solution Analytical Technology Co., Ltd., Wuhan, China. Analytical conditions were: an accelerating voltage of 15 kV, and a beam current of 2×10^{-8} A, a beam diameter of 2 μm. Counting times were 20 s on peaks, with 10 s on backgrounds. Data correction was processed by using a ZAF method. Fe^{3+} was calculated by charge balance. The analysis results are shown in Table 1. X-ray mapping was performed using an accelerating voltage of 20 kV, a beam current of 5×10^{-8} A, a beam diameter of 0.3 μm and a dwell time of 50 ms.

Trace elements in garnet

Trace element analyses of garnets were conducted with LA–ICP–MS at the Wuhan Sample Solution Analytical Technology Co., Ltd., Wuhan, China. Detailed operating conditions of the laser ablation system, the ICP–MS instrument and the data reduction were as same as in Zong *et al.* (2017). Laser sampling was performed using a GeolasPro laser ablation system that consists of a COMPexPro 102 ArF excimer laser and a MicroLas optical system. An Agilent 7700e ICP–MS instrument was used to acquire ion-signal intensities. A 'wire' signal smoothing device was included in this laser ablation system (Hu *et al.*, 2015). Spot size and frequency of the laser were set to be 44 μm and 5 Hz, respectively. Trace element compositions of garnets were calibrated based on various reference materials (BHVO–2G, BCR–2G and BIR–1G) without using an internal standard (Liu *et al.*, 2008). An Excel–based software ICPMSDataCal was used to perform quantitative calibration for trace element analyses (Liu *et al.*, 2008).

Raman measurements

Micro-Raman measurements were performed on representative thick sections at the School of Earth Science and Resources, Chang'an University, using a HORIBA LabRam HR Raman microspectrometer. A frequency-doubled Nd:YAG laser with 532 nm excitation wavelength was used. A petrographic microscope Olympus (50 × objective) was used to focus the laser on the selected inclusions. Raman spectra in the ranges 100–4000 cm^{-1} were collected with an integration time of 10 s, and three accumulations. Data were processed using LabSpec v5.58.25 and the phases inside the inclusions were identified according to the data from the literature (Frezzotti *et al.*, 2012; Ferrero *et al.*, 2016, 2021b; Carvalho *et al.*, 2020; Gianola *et al.*, 2021).

Re-homogenization of nanogranitoids

Re-homogenization experiments of NIs were conducted following the procedure described in Bartoli *et al.* (2013a), using a piston cylinder apparatus at the CAS Key Laboratory of Crust-Mantle Materials and Environments, University of Science and Technology of China and the QUICKpress non – endloaded piston cylinder available at the Laboratory of Experimental Petrology and Geochemistry, Dipartimento di Geoscienze, Università di Padova. During each run, separated garnet grains were charged into Au capsules with external diameters of 3–5 mm and length of 5–10 mm. They were alternated by powdered silicon dioxide. The experiments were performed under the following conditions: 1000°C and 6 hours, 950°C and 4 hours, 950°C and 2 hours, and 950°C and 1 hour. A fixed pressure of 12 kbar was adopted during the experiments.

Major elements in nanogranitoids

Major element compositions of the re-homogenized NIs were determined using a JEOL JXA 8530F plus EPMA at the CAS Key Laboratory of Crust-Mantle Materials and Environments, University of Science and Technology of China, Hefei, China. During EMPA analysis of hydrous granitic glasses, migration and loss of alkali from the inclusions may happen in the case that small beam sizes and high beam currents are adopted (e.g. Cesare *et al.*, 2015). To minimize the alkali loss, K_2O and Na_2O were determined at first. An anhydrous glass B (Morgan VI & London, 2005) was analyzed to obtain correction coefficients, which were used to correct the data of the unknown glasses. Analytical conditions were set as: a 15 kV accelerating voltage, a 5 nA beam current, variable beam diameters of 2–5 μm and counting times of 10 s on peak and 5 s on backgrounds.

Trace elements in nanogranitoids

Trace elements in NIs were analyzed at the State Key Laboratory for Mineral Deposit Research, Nanjing University, using a Coherent GeolasHD system equipped with a 193 nm excimer laser coupled to a NexION 350 ICP mass spectrometer (Pan *et al.*, 2019). The samples were loaded and analyzed in an in-house rhomb-shaped plexiglass cell of relatively small internal volume to enable fast washout of aerosol. The He-based aerosol was admixed with nebulizer gas via a T-junction prior to injection into the plasma. The ICP–MS was tuned to achieve maximum sensitivity and low oxide production rate by lowering the ThO/Th ratios to <0.5% before analyses. The analyzed inclusions are 2–25 μm beneath the surface to ensure they were representative of the original melts. The NIs close to the surface (2–10 μm in depth) were preferentially selected for analyses. In the rare case of deep-seated inclusions (15–25 μm in depth), the host garnet next to the inclusion was also analyzed and the ablation signal from the same depth interval as the inclusion was integrated, which will minimize the down-hole fractionation of elements during ablation (Zajacz & Halter, 2007). Repetition rate of the laser was increased to 10 Hz, on−sample energy densities of 5 J/cm^2 and spot size of 24 or 32 μm based on the size of NIs. Generally, measurement of each melt inclusion consists of 20–30 s instrumental background followed by 50–80 s ablations depending on the depth of melt inclusion. The glass NIST SRM 610 was employed as external standard. For the analyses of the NIST SRM 610, the spot size and energy density were set as 32 μm and 5 J/cm^2, respectively. The acquired time-resolved signals were processed using the software SILLS (Guillong *et al.*, 2008). Due to the small size of NIs, part of the host garnet has also been ablated along with target inclusions. Therefore, deconvolution of the resulting mixed garnet–glass signal was applied following the procedures of Halter *et al.* (2002). The Al_2O_3 of the re-homogenized inclusions derived from EPMA was adopted as reference standards for inclusions and garnet hosts, and MgO was used as the matrix−only tracer. Uncertainties and calculated limits of detection increase with the concentrations of elements in the host, thus, some elements which are strongly compatible in the host garnets (e.g. Y, Gd, V, Zn, Sc and heavy rare earth elements−HREEs) are normally not detectable in the inclusions. Some inclusions show anomalously high concentrations of Zr, Th, U, Nb and Sr, suggesting the occurrence of accidental trapped phases (e.g. zircon, monazite, rutile and apatite) (Bartoli *et al.*, 2019). For these inclusions with extremely high contents of Zr, Th, U, Nb and Sr, only Rb, Cs, Ba and Li are reported in Table 4 and discussed in the text.

U–Pb dating of zircon

Conventional magnetic and heavy liquid techniques followed by hand-picking under a binocular microscope were used for separation of zircons from the Mather *UHT* metapelitic granulites.

Table 1: Representative mineral compositions of the Mather *UHT* granulites. The major element compositions are shown in wt.%

	Grt-c	Grt-m	Grt-r	Grt_3	$Opx_{in\ Grt}$	Opx-c	Opx-r	$Opx_{exsolved}$	Opx_{inter}	Opx_3	$Spr_{with\ Crd}$	$Spr_{with\ Bt}$	Crd_{inter}	$Bt_{in\ Grt}$	Bt_{porphy}	Bt_{inter}	Bt-3	Pl_{inter}	Pl_3	Spl	Pl-in Zrn	Bt-in Zrn	Opx-in Zrn
SiO_2	40.94	40.51	40.63	39.94	51.14	52.34	49.11	51.07	50.20	50.68	13.27	13.41	49.20	39.71	36.67	36.69	37.48	47.03	55.19	0.04	59.87	38.51	50.28
TiO_2	0.03	0.06	0.00	0.00	0.04	0.07	0.08	0.11	0.09	0.06	0.05	0.10	0.03	3.47	4.08	4.32	4.12	0.00	0.00	0.04	0.01	3.54	0.05
Al_2O_3	23.23	23.01	23.11	22.38	8.85	6.49	9.16	6.88	7.37	7.67	62.22	61.34	34.03	15.49	16.93	17.13	16.88	33.73	29.04	61.11	24.95	16.96	6.79
Cr_2O_3	0.12	0.10	0.09	0.01	0.10	0.03	0.03	0.07	0.12	0.07	0.32	0.49	0.06	0.09	0.13	0.25	0.10	0.00	0.00	1.28	0.06	0.08	0.11
Fe^TO	17.26	18.17	19.73	23.84	12.04	13.06	14.93	15.21	15.24	15.49	7.79	8.51	2.61	5.44	8.25	8.92	8.68	0.24	0.25	21.85	0.03	11.53	17.62
MnO	0.18	0.16	0.26	0.38	0.04	0.03	0.10	0.07	0.08	0.11	0.04	0.06	0.03	0.00	0.02	0.00	0.01	0.02	0.01	0.08		0.06	0.08
MgO	16.87	15.96	15.00	11.81	27.31	27.61	25.58	26.23	27.00	25.17	16.26	16.70	12.60	21.90	18.24	17.79	18.16	0.00	0.13	12.71	0.00	15.58	24.69
CaO	1.47	1.18	1.63	1.78	0.10	0.09	0.11	0.12	0.09	0.07	0.00	0.02	0.03	0.02	0.02	0.00	0.00	16.46	10.40	0.00	7.15	0.00	0.10
Na_2O	0.01	0.03	0.02	0.02	0.05	0.00	0.00	0.03	0.02	0.04	0.02	0.00	0.04	0.43	0.44	0.33	0.41	2.14	5.33	0.08	7.24	0.12	0.01
K_2O	0.00	0.00	0.00	0.01	0.00	0.00	0.01	0.00	0.00	0.03	0.00	0.00	0.01	9.46	9.96	9.52	9.85	0.03	0.53	0.02	0.16	8.56	0.00
ZnO	–	–	–	–	–	–	–	–	–	–	–	–	–	–	–	–	–	–	–	1.37	–	–	–
F	–	–	–	–	–	–	–	–	–	–	–	–	–	0.37	0.09	0.29	0.22	–	–	–	–	–	–
Cl	–	–	–	–	–	–	–	–	–	–	–	–	–	0.10	0.12	0.11	0.12	–	–	–	–	–	–
Total	100.11	99.18	100.47	100.17	99.67	99.72	99.09	99.79	100.21	99.39	99.97	100.63	98.63	96.49	94.94	95.34	96.03	99.66	100.87	98.58	99.52	94.95	99.72
O	12	12	12	12	6	6	6	6	6	6	20	20	18	11	11	11	11	8	8	4	8	11	6
Si	2.984	2.995	2.987	3.009	1.815	1.864	1.773	1.834	1.791	1.833	1.578	1.587	4.921	2.802	2.681	2.676	2.710	2.165	2.468	0.001	2.679	2.807	1.826
Ti	0.002	0.003	0.000	0.000	0.001	0.002	0.002	0.003	0.002	0.002	0.004	0.009	0.002	0.184	0.224	0.237	0.224	0.000	0.000	0.001	0.000	0.194	0.001
Al	1.996	2.005	2.003	1.988	0.370	0.272	0.390	0.291	0.310	0.327	8.723	8.561	4.012	1.289	1.459	1.472	1.439	1.831	1.531	1.936	1.316	1.458	0.291
Cr	0.007	0.006	0.005	0.001	0.003	0.001	0.001	0.002	0.003	0.002	0.030	0.046	0.005	0.005	0.008	0.015	0.006	0.000	0.000	0.027	0.002	0.004	0.003
Fe^{3+}	0.028	0.000	0.020	0.000	0.000	0.000	0.060	0.035	0.091	0.005	0.087	0.201	0.044	0.000	0.000	0.000	0.000	0.009	0.009	0.037	0.001	0.000	0.051
Fe^{2+}	1.024	1.123	1.193	1.502	0.357	0.389	0.391	0.422	0.364	0.464	0.688	0.642	0.175	0.321	0.504	0.544	0.525	0.000	0.000	0.456	0.000	0.703	0.484
Mn	0.011	0.010	0.016	0.024	0.001	0.001	0.003	0.002	0.002	0.003	0.004	0.006	0.003	0.000	0.001	0.000	0.001	0.001	0.000	0.002	0.001	0.004	0.002
Mg	1.832	1.758	1.644	1.326	1.444	1.465	1.376	1.404	1.436	1.357	2.882	2.946	1.878	2.303	1.987	1.934	1.957	0.000	0.009	0.509	0.000	1.692	1.337
Ca	0.115	0.093	0.128	0.144	0.004	0.003	0.004	0.005	0.003	0.003	0.000	0.003	0.003	0.002	0.002	0.000	0.000	0.812	0.498	0.000	0.343	0.000	0.004
Na	0.001	0.004	0.003	0.003	0.003	0.000	0.000	0.002	0.001	0.003	0.005	0.000	0.008	0.058	0.063	0.047	0.058	0.191	0.462	0.004	0.628	0.017	0.000
K	0.000	0.000	0.000	0.001	0.000	0.000	0.000	0.000	0.000	0.001	0.000	0.000	0.001	0.852	0.929	0.885	0.909	0.002	0.030	0.001	0.009	0.796	0.000
Zn	–	–	–	–	–	–	–	–	–	–	–	–	–	–	–	–	–	–	–	0.027	–	–	–
F	–	–	–	–	–	–	–	–	–	–	–	–	–	0.08	0.02	0.07	0.05	–	–	–	–	–	–
Cl	–	–	–	–	–	–	–	–	–	–	–	–	–	0.01	0.02	0.01	0.02	–	–	–	–	–	–
Total	8.000	7.997	7.999	7.998	3.998	3.997	4.000	4.000	4.003	4.000	14.001	14.001	11.052	7.911	7.893	7.888	7.893	5.011	5.007	3.002	4.979	7.675	3.999
Alm	34	38	40	50																			
X_{Mg}	0.64	0.61	0.58	0.47	0.80	0.79	0.78	0.77	0.80	0.75	0.81	0.82	0.91	0.88	0.80	0.78	0.79			0.53		0.71	0.73
X_{An}																		0.81	0.50		0.35		

Abbreviations: c, core; m, mantle; r, rim; in, inclusions; inter, intergrowth; porphy, porphyroblast; 3, minerals formed at M3 stage.

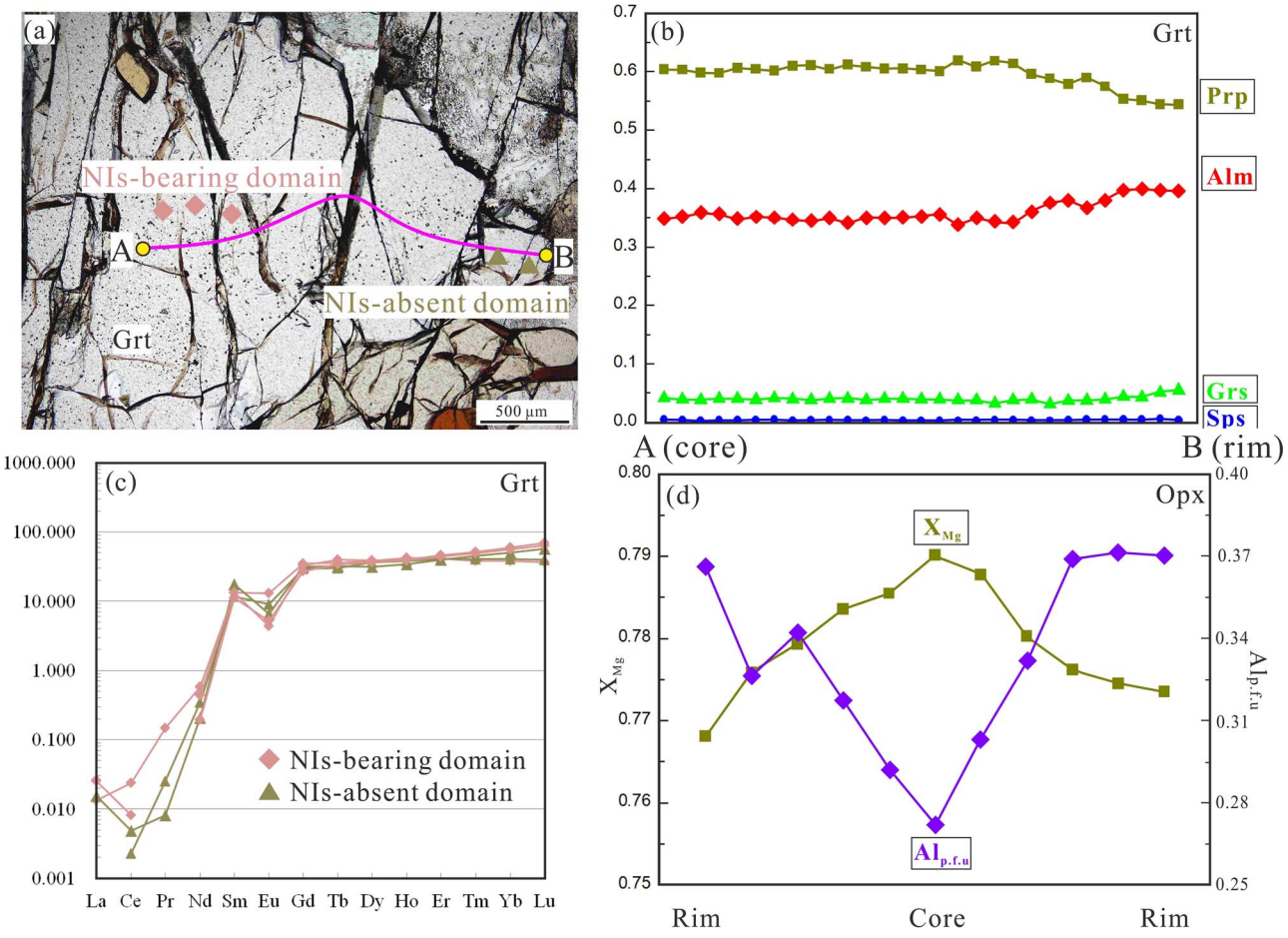

Fig. 4. (a) Garnet grain showing the analysis positions. (b) Compositional zoning profile across garnet from core to rim. (c) Chondrite-normalized REE patterns of garnets for the NI-bearing and NI-absent domains. (d) Compositional zoning profiles across an orthopyroxene porphyroblast.

Morphology and internal structure of the zircons were documented with transmitted, reflected light microphotographs and cathodoluminescene (CL) images. Zircon U–Pb dating was carried out using LA–ICP–MS at the Wuhan Sample Solution Analytical Technology Co., Ltd., Wuhan, China. Detailed operating conditions for the laser ablation system and the ICP–MS instrument and data reduction were described in Zong *et al.* (2017). Laser sampling was performed using a GeolasPro laser ablation system that consists of a COMPexPro 102 ArF excimer laser (wavelength of 193 nm and maximum energy of 200 mJ) and a MicroLas optical system. Each analysis incorporated a background acquisition of approximately 20–30 s followed by 50 s of data acquisition from the sample. Spot size and frequency of the laser for analyses were set to 24 mm and 10 Hz, respectively. Zircon 91500 and glass NIST610 were used respectively as external standards for U–Pb dating and trace element calibrations. In order to monitor the external uncertainties of zircon dating, a zircon standard GJ – 1 was alternately analyzed together with the other unknown zircons. Fourteen measurements of the zircon GJ – 1 yielded a weighted mean $^{206}Pb/^{238}U$ age of 602.1 ± 4.4 Ma (MSWD = 0.22), which is roughly in agreement with the recommended $^{206}Pb/^{238}U$ age value of 600.4 ± 0.6 Ma (Jackson *et al.*, 2004). An Excel-based software ICPMSDataCal was used to perform off-line selection and integration of background and analyzed signals, time-drift correction and quantitative calibration for trace element analyses and U–Pb dating (Liu *et al.*, 2010). Programs SQUID 1.0 and ISOPLOT (V.3.0; Ludwig, 1999) were used for data processing.

RESULTS

Mineral chemistry

Garnet porphyroblasts are chemically homogeneous from core to mantle ($Alm_{34–38}Prp_{59–62}Grs_{3–4}Sps_{0–1}$). Small garnet crystals and garnet porphyroblast rims have slightly lower pyrope contents, with compositions of $Alm_{40–46}Prp_{55–56}Grs_{4–3}Sps_{0–1}$ (Fig. 4a, b). The garnet relicts from the strongly deformed domain display the lowest magnesium contents ($Alm_{48–50}Prp_{46–44}Grs_{4–5}Sps_{0–1}$). NI–bearing and NI-absent domains display similar REE patterns in the chondrite–normalized diagram, with enrichments of HREEs and slightly negative Eu anomalies (Fig. 4c).

Orthopyroxene porphyroblasts preserve evident Al-zoning patterns, with y_{Al} (= $Al^{IV} = Al/2$) values increasing from 0.14 ($Al_2O_3 = \sim 6.49$ wt.%) in the core to 0.19 ($Al_2O_3 = \sim 8.79$ wt.%) in the rim (Fig. 4d). The highest Al_2O_3 content of orthopyroxene detected in the sample is ~9.16 wt.%, with corresponding y_{Al} value of 0.19. However, orthopyroxene porphyroblasts show relatively restricted X_{Mg} ($X_{Mg} = Mg/(Mg + Fe^{2+})$) variations (0.77–0.79). Orthopyroxene inclusions in garnet have Al_2O_3 contents of 8.85–9.04 wt.% ($y_{Al} = \sim 0.19$) and X_{Mg} values of 0.78–0.80. Orthopyroxene from the orthopyroxene–cordierite symplectites have y_{Al} of 0.14–0.16 and X_{Mg} of 0.75–0.80. Vermicular low-Al orthopyroxene in the rims of some orthopyroxene porphyroblasts displays Al_2O_3 contents of ~6.88 wt.% ($y_{Al} = \sim 0.15$) and X_{Mg} values of ~0.77. Orthopyroxene grains associated with the retrograde biotite display Al_2O_3 contents of 7.67–7.69 ($y_{Al} = 0.16–0.17$) and X_{Mg} of 0.74–0.76.

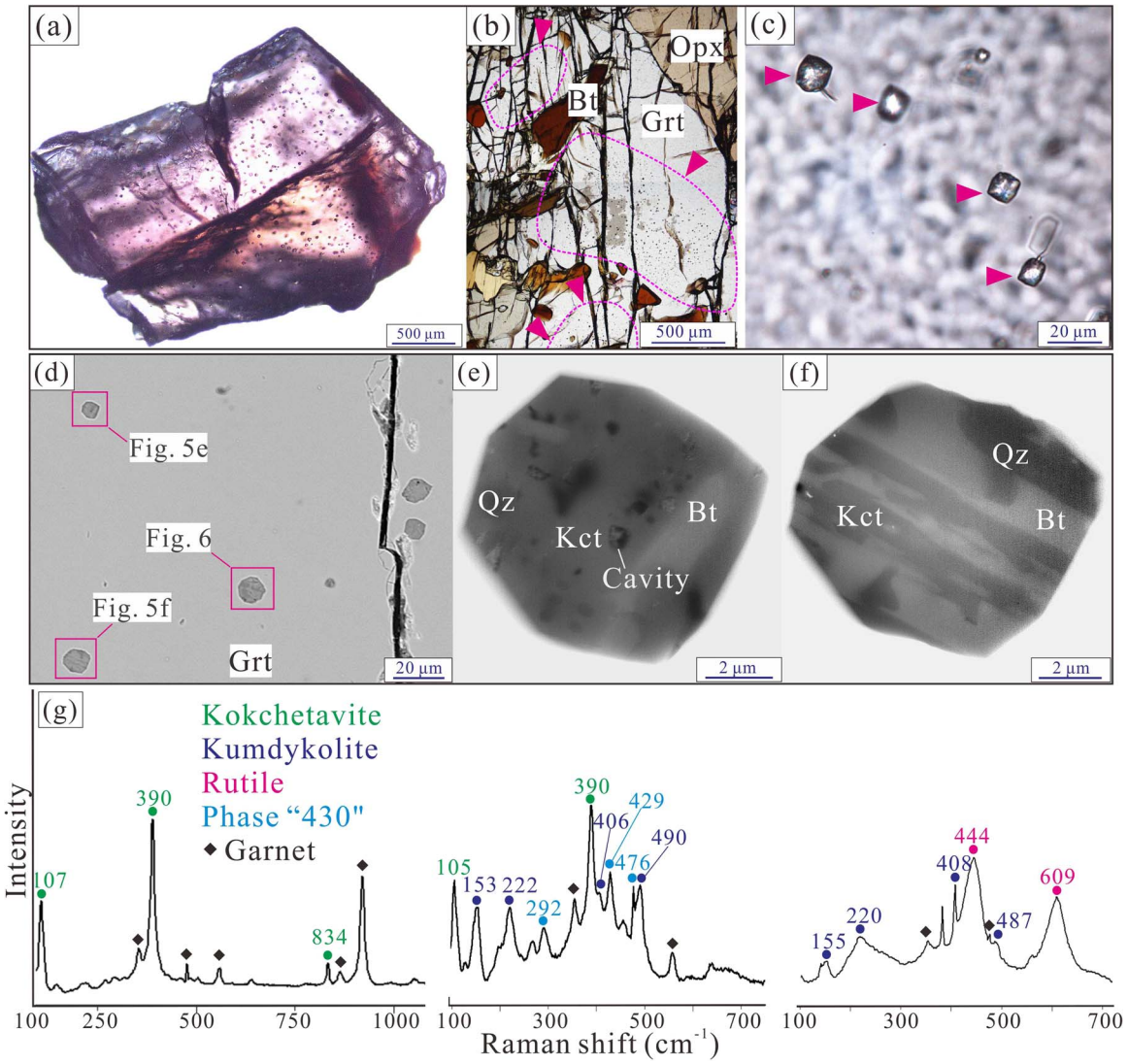

Fig. 5. Plane polarized light photomicrographs and BSE images of NIs within garnet porphyroblasts and Raman spectrum of these inclusions. (a) Garnet crystal mounted on an epoxy resin disc containing abundant NIs. (b,c) Plane polarized photomicrographs showing NIs within peritectic garnets. (d–f) BSE images showing NIs with daughter phases of quartz, biotite and kokchetavite. Some cavities are also observed and might be related to the exsolution of fluid during the retrograde crystallization of melt. (g) Mixed Raman spectrum of NIs and their garnet hosts.

Biotite porphyroblasts show relatively homogeneous compositions, with TiO_2 contents of 4.29–4.61 wt.% and X_{Mg} of 0.79–0.81. The low TiO_2 contents for peak biotite can be partially ascribed to crystal-chemical constraints, which hamper the temperature control on Ti content of biotite (Cesare *et al.*, 2008). Biotite inclusions within garnet have relatively higher X_{Mg} values (0.84–0.87) than those within orthopyroxene (~0.79). However, they show similar TiO_2 content variations ranging from 2.90 to 4.46 wt.%. The retrograde biotite has TiO_2 contents of ~2.63 wt.% and X_{Mg} values of ~0.81. Halogen concentrations in the analyzed biotite crystals are undistinguishable, with F and Cl contents of 0.09–0.37 wt.% and 0.10–0.12 wt.%, respectively.

Sapphirine associated with retrograde biotite has slightly higher X_{Mg} values (0.84–0.86) than that from sapphirine–cordierite intergrowths (0.80–0.82), both of which show indistinguishable Fe^{3+}/Fe^{T} ratios varying from 0.71 to 0.81. Cordierite grains from different positions show restricted X_{Mg} variations from 0.90 to 0.92. Spinel has X_{Mg} of 0.43–0.48 and ZnO contents of 0.64–1.72 wt.%. Plagioclase from the orthopyroxene–cordierite intergrowths is rich in anorthite, with a typical X_{An} (= Ca/(Ca + Na + K)) of ~0.81. However, plagioclase associated with the retrograde biotite has lower X_{An} values of 0.51–0.58.

Microstructures of melt and fluid inclusions

Nanogranitoids are randomly distributed within garnet crystals, but absent in the outer rims (Figs 3a, 4a, 5a). They are also absent in the small garnet crystals from the strongly deformed domains (Fig. 3i). These inclusions show spherical or polygonal shape, and are 5–15 μm in size (Figs 5b–f, 6). They usually display negative crystal shapes, and may contain nano-scale porosities (Fig. 5e), implying the possible presence of fluid which was dissolved in the former melts and subsequently exsolved upon crystallization (Bartoli *et al.*, 2013b). Coupled Raman analyses and compositional maps suggest that they contain daughter phases of quartz, kokchetavite ($KAlSi_3O_8$), minor kumdykolite ($NaAlSi_3O_8$) and biotite (Figs 5g, 6), indicating the former presence of silicate melts. Moreover, an unknown phase with Raman peaks at 292, 429 and 476 cm^{-1} has also been detected (Fig. 5g). Such phase has been previously recognized within garnet–hosted melt inclusions from the Gruf Complex (Gianola *et al.*, 2021) and the Central Maine

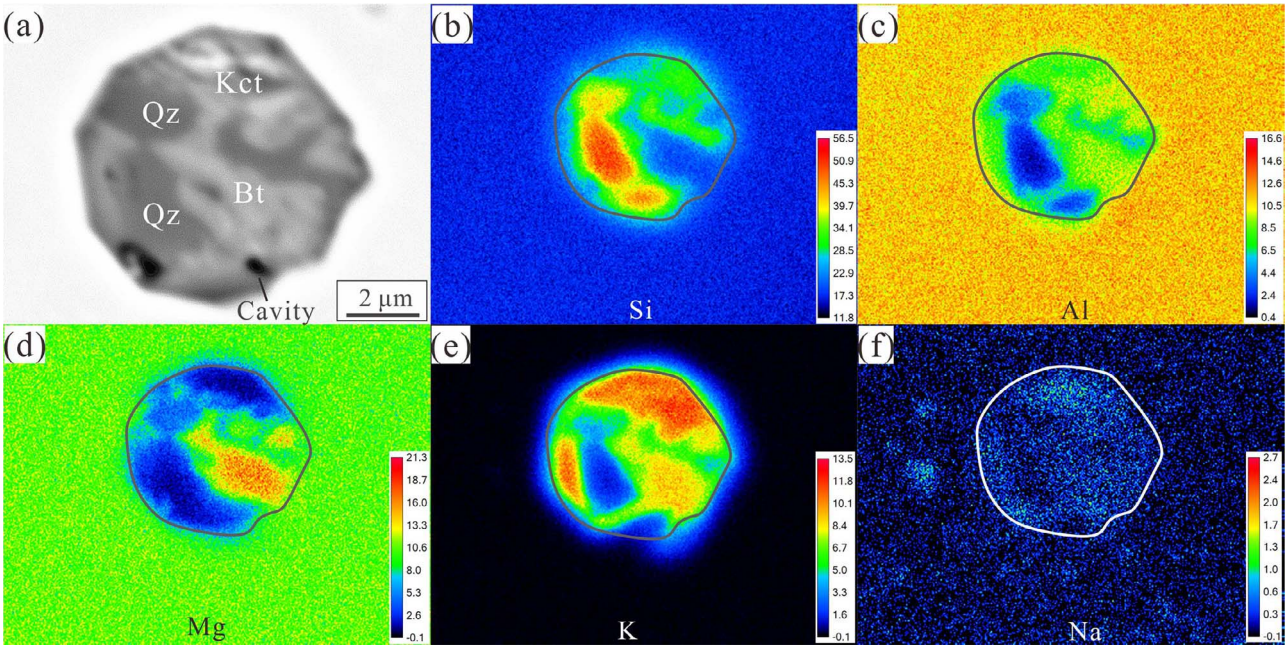

Fig. 6. A BSE image of a nanogranitoid inclusion and corresponding X-ray maps of Si, Al, Mg, K and Na.

Terrane (Ferrero *et al.*, 2021b). This phase was described as phase '430' by Ferrero *et al.* (2021b). Apatite, rutile, zircon and monazite may be present as accidentally trapped phases, as indicated by the relatively large size of trapped phases compared with the size of the melt inclusions, and also by their low solubility in granitic melts (e.g. Bartoli *et al.*, 2019). Daughter biotite crystals in NIs have very low TiO_2 contents of 0.03–0.50, and is characterized by high X_{Mg} values ranging from 0.92 to 0.95, whereas F and Cl contents in biotite are negligible, lower than 0.07 and 0.03 wt.%, respectively. Kokchetavite has a typical composition of $Or_{94}Ab_6$ and kumdykolite displays compositions of $Or_5An_8Ab_{87}$. For detailed mineral compositions, please refer to Table 2.

Fluid inclusions are also found within garnet (Figs 3a, 7a, b) and orthopyroxene (Fig. 7c). These fluid inclusions display granular or vermicular shapes, with sizes of 5–40 μm (Fig. 7). They are usually present along healed cracks, suggesting that they are secondary in origin. Some early trapped fluid has reacted with their hosts to produce stepdaughter phases (i.e. their precipitation results from fluid–host interaction; Carvalho *et al.*, 2020) of pyrophyllite, magnesite, corundum and quartz, with or without residual CO_2 (Fig. 7d, e). The measured CO_2 Fermi diad splits range from 102.8 to 105.1 cm^{-1}, corresponding to densities of 0.2–1.0 g/cm^3 calculated with the densimeter of Wang *et al.* (2011). Secondary pure CO_2 inclusions may also occur along healed garnet cracks (Fig. 7f), which have a density of ~0.8 g/cm^3. Although not detected in this study, the existence of trace amounts of free H_2O cannot be precluded because H_2O-rich liquid may be present as a thin film (<0.1 μm) wetting the walls of the FIs at ambient conditions (e.g. Berkesi *et al.*, 2009; Lamadrid *et al.*, 2014). Other fluid species such as N_2 and CH_4 have not been detected in this study.

Table 2: Compositions of daughter phases within NIs. The major element compositions are shown in wt.%

	Bt	Kok	Kum
SiO_2	39.22	75.17	66.34
TiO_2	0.50	0.00	0.03
Al_2O_3	19.22	11.89	19.5
Cr_2O_3	0.18	0.00	0.01
Fe^TO	2.88	0.75	0.83
MnO	0.02	0.03	0
MgO	23.88	0.04	1.67
CaO	0.06	0.02	1.46
Na_2O	0.73	0.44	8.38
K_2O	9.29	10.85	0.71
F	0.00	–	–
Cl	0.02	–	–
Total	95.99	99.21	98.93
O	11	8	8
Si	2.729	3.345	2.934
Ti	0.026	0.000	0.001
Al	1.576	0.624	1.017
Cr	0.010	0.000	0.000
Fe^{3+}	0.025	0.028	0.031
Fe^{2+}	0.142	0.000	0.000
MnO	0.001	0.001	0.000
Mg	2.477	0.003	0.110
Ca	0.004	0.001	0.069
Na	0.098	0.038	0.719
K	0.824	0.616	0.040
F	0.000	–	–
Cl	0.002	–	–
Total	7.914	4.656	4.921
X_{Mg}	0.95		
X_{An}		0.94	0.08

Microstructures of re – homogenized nanogranitoids

Experiments at 950°C with run durations of 2–4 hours yielded some homogenized melt inclusions. However, those at 950°C with run duration of 1 hour produced the largest proportion of perfectly re – homogenized inclusions (Fig. 8). Some inclusions show clear evidence for overheating, such as the occurrences of (1) irregular boundaries between inclusions and garnet hosts (Fig. 8a); (2) secondary minerals (i.e. orthopyroxene) formed during experiments or upon quenching (Fig. 8a–d); (3) new growth of garnet on the

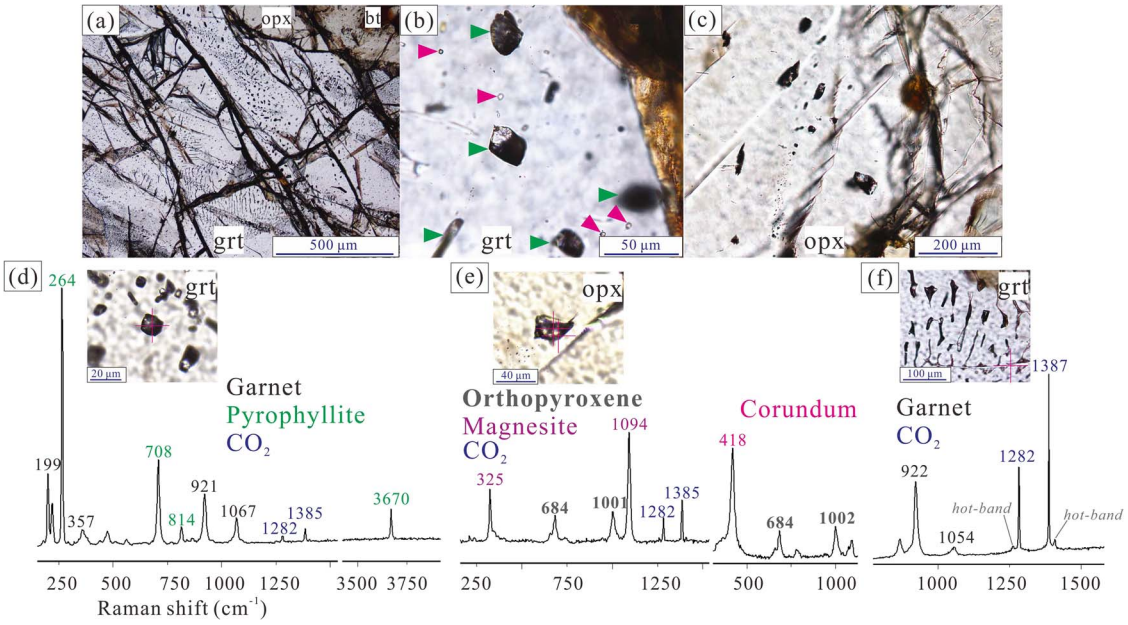

Fig. 7. (a–c) Secondary FIs within garnet and orthopyroxene porphyroblasts. Pink and green arrows respectively point to nanogranitoid and fluid inclusions, where NIs are randomly distributed while FIs are mostly present along the cracks. (d–f) Mixed spectra of FIs and their hosts.

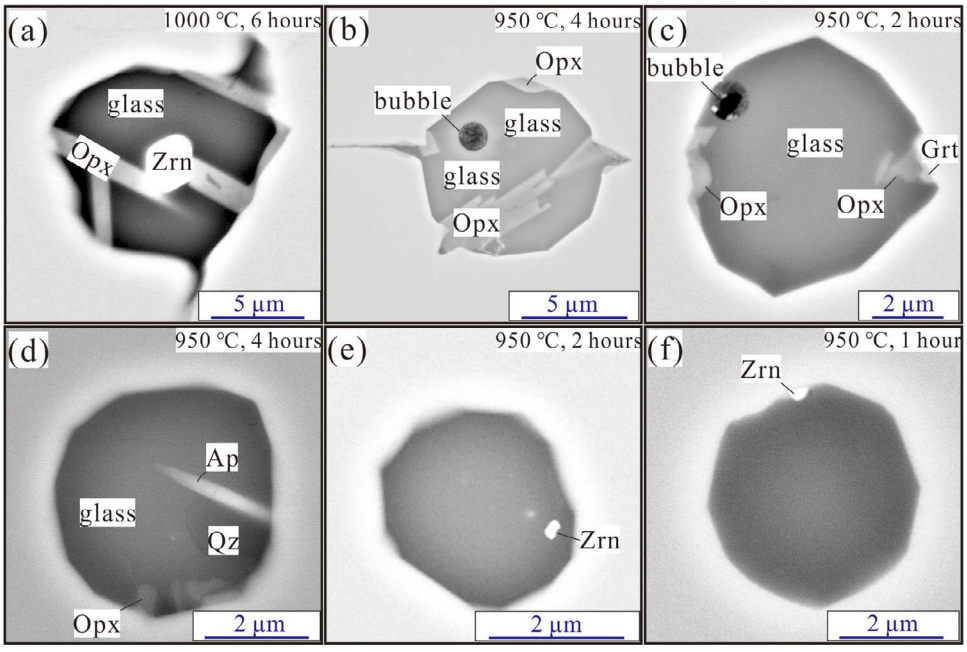

Fig. 8. BSE images of experimentally re-homogenized NIs under 1000°C and 12 kbar with a run duration of 6 hours (a), 950°C and 12 kbar with run durations of 4 hours (b, d), 2 hours (c, e), and 1 hour (f). Perfectly re-homogenized inclusions with well-developed negative shapes are shown in (e) and (f). Other inclusions show clear evidence for overheating (a–d).

inclusion walls (Fig. 8c); and (4) offshoots around melt inclusions formed as a consequence of decrepitations (Fig. 8a, b). The compositions of these inclusions showing interaction with the host have been disregarded. Shrinkage bubbles have also been observed within the overheated inclusions (Fig. 8b, c), suggesting that the fluid may have undergone incomplete dissolution in the melts during the experimental run or, alternatively, it diffused during cooling to form shrinkage bubbles (Lowenstern, 1995; Bartoli *et al.*, 2013a). Some inclusions were not re – homogenized properly during the experiments, as indicated by the coexistence of melts with rounded residual quartz (Fig. 8d). Some melt inclusions still contain accessory minerals such as apatite, rutile, zircon and monazite (Fig. 8a, d–f). This strongly indicates that these phases are accidentally trapped minerals (Ferrero *et al.*, 2012).

Major element compositions of re-homogenized nanogranitoids

Re-homogenized inclusions are strongly peraluminous (ASI = $[Al_2O_3/(CaO + Na_2O + K_2O)] = 1.24–1.61$) (Fig. 9) and rhyolitic in composition, with high SiO_2 contents of 69.89–75.61 wt.%, high $Na_2O + K_2O$ contents of 7.08–9.53 wt.% (K/Na = 2.21–9.31) and extremely low CaO (< 0.7 wt.%) and FeO + MgO contents (Table 3).

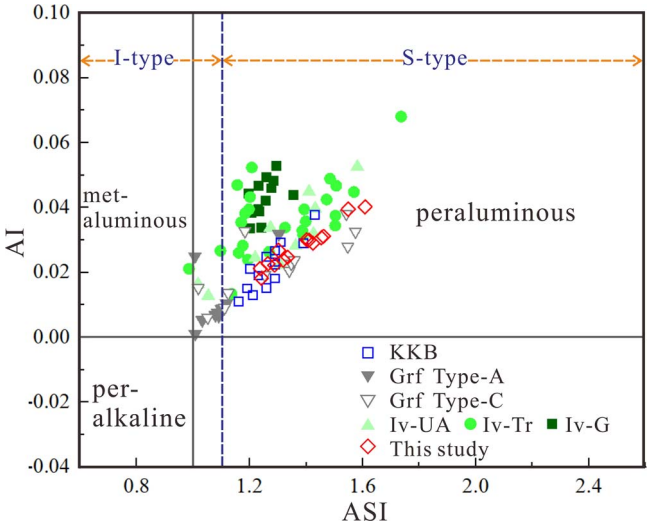

Fig. 9. Plot of aluminum saturation index vs. alkalinity index [AI = molar $Al_2O_3 - (Na_2O + K_2O)$ (from Frost & Frost, 2008). Dotted line separates the compositional fields of I- and S-type granites (from Chappell, 1999). KKB, Kerala Khondalite Belt (India) (Cesare *et al.*, 2009; Ferrero *et al.*, 2012), with peak *P–T* conditions of 900°C and 6–8 kbar (Cenki *et al.*, 2002; Shabeer *et al.*, 2005); Grf Type-A and -C, type-A or -C granulites from the Gruf Complex (European Central Alps) (Gianola *et al.*, 2021), with peak *P–T* conditions of 920–940°C and 8.5–9.5 kbar (Galli *et al.*, 2012); Iv, metapelitic migmatites from the Ivrea Zone (NW Italy) (Carvalho *et al.*, 2019), with *P–T* conditions of 650–730°C and 3.5–6.5 kbar for the UA, and 900–950°C and 11–12 kbar for the G (Ewing *et al.*, 2013; Redler *et al.*, 2013). UA, upper amphibolite facies zone; Tr, transition zone; G, granulite facies zone.

Difference of EMPA totals from 100% suggest that the H_2O contents in the analyzed MIs are 1.49 to 4.24 wt.%, with an average value of 2.79 wt.%.

In the CIPW-normative Qz–Ab–Or diagram (Fig. 10a), the high-SiO_2, potassic to ultrapotassic melts plot far away from haplogranitic minimum melts, and define an elongated trend paralleling to the Qz–Or sideline, which are consistent with the melt compositions found in other *UHT* occurrences reported by Cesare *et al.* (2009), Gianola *et al.* (2021) and Ferrero *et al.* (2012). Similar compositions have also been obtained by melting experiments of pelitic protoliths at 5–7 kbar and 900–950°C (Patiño Douce & Johnston, 1991; Droop *et al.*, 2003) (Fig. 10a). In the Ab–An–Or diagram, the NIs show variable Or/Ab ratios and low An contents. They plot in the granite field, and are close to the boundary between granite and Qz–monzonite (Fig. 10b).

Trace element compositions of nanogranitoids

In the average upper continental crust (UCC) normalized diagram (Rudnick & Gao, 2014), NIs from the Mather Peninsula are enriched in Rb, Sm, Ta and depleted in Ba, Pb, Th, Ce and Sr (Fig. 11). Compared with the granulitic restite (i.e. granulites that have experienced partial melting and substantial melt loss), NIs are enriched in Li (5.3–76.9 ppm), Cs (0.9–35.5 ppm), Rb (126.7–1325.0 ppm), Ta (1.4–3.2 ppm), Sm (5.5–27.2 ppm), Zr (84.2–276.5 ppm), Nd (7.2–22.8 ppm), and depleted in Ce (2.4–13.4 ppm), Th (0.4–3.8 ppm), Ba (56.3–565.6 ppm), Sr (5.8–27.6 ppm) and Nb (4.0–15.7 ppm) (Table 4; Fig. 11). The melts have relatively higher U (0.6–9.3 ppm) and Pb contents (3.9–12.8 ppm), and display higher Rb/Sr (7.69–52.08) and Sm/Nd (0.52–1.14) ratios relative to the granulitic restite (Rb/Sr = ~8.56; Sm/Nd = ~0.25). They also contain variable amounts of Sc (9.7–42.0 ppm), V (29.4–146.6 ppm) and Zn (83.3–130.7 ppm), which are discarded in this study because these concentrations might be affected by contamination from the garnet hosts (Bartoli *et al.*, 2019).

Zircon morphology, U–Pb dates and trace elements

Zircon grains from the Mather *UHT* metapelitic granulites are usually rounded, and have grain sizes of 80–250 μm. They typically display complex core–mantle–rim structures and occasionally, they may be homogeneous in the CL images (Fig. 12a). The cores are generally 30–120 μm in diameter, and show oscillatory zoning or homogeneous patterns. Most zircon cores are enclosed by dark–grey mantles, which usually show blurred zoning or are unzoned. Sometimes, zircon cores and mantles are enveloped by pale–grey to bright rims (Fig. 12a). A total of 46 analyses of zircon were conducted on 34 grains. Zircon cores yield inherited $^{207}Pb/^{206}Pb$ dates of 2623–2088 Ma (N = 13; Th/U = 0.28–1.81). Zircon mantles document $^{206}Pb/^{238}U$ dates ranging from 1050 to 607 Ma (N = 27; Th/U = 0.01–0.09) while the rims record $^{206}Pb/^{238}U$ dates varying from 569 to 472 Ma (N = 6; Th/U = 0.11–0.34) (Table 5).

Orthopyroxene, biotite, plagioclase, apatite, chlorite, quartz and monazite inclusions were observed within zircons (Fig. 12c). Some trivial inclusions are extensively present along the healed fractures in zircons (Fig. 12b, d). They cannot be analyzed due to their small sizes. However, their appearance resembles FIs reported in literature (Fig. 6d in Li *et al.*, 2018). Thus, these inclusions are suspected to also be FIs. Accordingly, the large variations of U–Pb dates for zircon mantles and rims (Fig. 12e) and Pb loss could result from extensive fluid infiltration and the Pan–African *HT–UHT* overprinting. Zircon cores are characterized by the presence of low-Mg biotite (X_{Mg} = ~0.71) and low-Ca plagioclase (X_{An} = ~0.35) inclusions (Table 1), which were not found in the matrix, suggesting that these cores are detrital in origin. It is worth noting that an orthopyroxene grain enclosed in a detrital zircon (i.e. it shows a near concordant date of ~2381 Ma) shows high Al_2O_3 contents of ~6.79 wt.% (Fig. 12c), indicative of a possible high-grade metamorphism in the Paleoproterozoic.

PHASE EQUILIBRIA MODELING

Phase equilibria modeling for the Mather *UHT* metapelitic granulite sample (RG16–80) was conducted with Perple_X (v. 6.9.1; Connolly, 2005) and the ds622 thermodynamic data set (Holland & Powell, 2011). Pseudosections were calculated in the 11-component MnO–Na_2O–CaO–K_2O–FeO–MgO–Al_2O_3–SiO_2–H_2O–TiO_2–O_2 (MnNCKFMASHTO) system. This system is considered to provide a realistic approximation to the composition of the samples within which melt and Fe^{3+} can be assessed. The solution model for sapphirine is from Wheller & Powell (2014) and *a–x* models for other phases are same to those adopted by White *et al.* (2014). Whole-rock composition of a piece of relatively homogeneous rock ($5 \times 5 \times 3$ cm^3), obtained from XRF analysis, was used as the bulk rock composition for the modeling. The formation of fine-grained intergrowths is usually controlled by local effective bulk compositions. In this study, we assume that whole-rock composition obtained from XRF can roughly represent the local effective bulk composition of the symplectite formation. The H_2O contents were adjusted to ensure that the final assemblage is stable just above the solidus (Korhonen *et al.*, 2012). A preliminary T–X(Fe_2O_3) diagram was calculated to evaluate the effect of Fe^{3+}contents on phase assemblage (Figure S1). Based on the predicted peak assemblages across the range of Fe^{3+} contents, a Fe^{3+}/Fe^{T} value of ~0.16 is finally adopted.

Table 3: Major element concentrations of re – homogenized NIs. The compositions are shown in wt.%

	1	2	3	4	5	6	7	8	9	10	11	12	13	14	ave.	σ	PEM
SiO_2	73.60	70.36	72.93	69.94	70.99	69.89	73.16	75.61	72.78	74.94	73.14	71.33	73.86	70.48	72.36	1.80	69.33
TiO_2	0.00	0.05	0.04	0.07	0.03	0.01	0.02	0.00	0.06	0.06	0.00	0.04	0.02	0.03	0.03	0.02	0.00
Al_2O_3	14.28	14.21	15.21	15.28	14.30	14.49	12.70	13.47	13.33	13.05	15.06	14.21	13.89	14.52	14.14	0.76	14.19
Cr_2O_3	0.00	0.04	0.00	0.00	0.00	0.02	0.00	0.01	0.00	0.00	0.00	0.03	0.00	0.02	0.01	0.01	0.00
Fe^TO	1.10	1.12	1.22	1.11	1.22	1.43	1.03	0.98	1.00	0.99	1.33	1.44	1.11	1.09	1.15	0.15	0.48
MnO	0.00	0.02	0.02	0.04	0.00	0.00	0.00	0.00	0.01	0.02	0.00	0.00	0.02	0.04	0.01	0.02	0.00
MgO	0.54	1.23	0.77	1.34	0.83	0.94	0.39	0.41	0.41	0.41	0.62	1.87	0.58	0.54	0.78	0.42	0.29
CaO	0.35	0.45	0.43	0.46	0.56	0.32	0.36	0.38	0.58	0.41	0.63	0.51	0.39	0.30	0.44	0.10	0.63
Na_2O	1.26	0.94	0.99	1.06	1.30	1.39	0.99	0.99	1.05	1.31	1.63	0.74	0.64	0.61	1.06	0.28	1.70
K_2O	6.53	8.43	6.50	8.47	6.47	7.52	7.33	6.60	7.15	6.68	5.46	7.40	7.20	8.62	7.17	0.86	8.53
Cl	0.05	0.05	0.06	0.05	0.06	0.04	0.06	0.06	0.06	0.05	0.06	0.04	0.08	0.02	0.05	0.01	0.00
P_2O_5	0.00	0.02	0.00	0.01	0.00	0.00	0.00	0.00	0.00	0.00	0.03	0.00	0.03	0.00	0.01	0.01	0.00
Total	97.71	96.91	98.18	97.84	95.76	96.05	96.04	98.51	96.44	97.92	97.95	97.61	97.80	96.29	97.21	0.89	96.29
H_2O by diff	2.29	3.09	1.82	2.16	4.24	3.95	3.96	1.49	3.56	2.08	2.05	2.39	2.20	3.71	2.79	0.89	4.85
ASI	1.46	1.24	1.61	1.30	1.41	1.32	1.24	1.42	1.26	1.29	1.55	1.40	1.45	1.33	1.40	0.11	1.08
AI	0.03	0.02	0.04	0.03	0.03	0.02	0.02	0.03	0.02	0.02	0.04	0.03	0.03	0.02	0.03	0.01	0.01
$Na_2O + K_2O$	7.79	9.37	7.49	9.53	7.77	8.91	8.32	7.59	8.21	7.99	7.08	8.14	7.84	9.23	8.23	0.72	10.23
K/Na	3.40	5.90	4.30	5.25	3.29	3.57	4.85	4.38	4.46	3.34	2.21	6.59	7.44	9.31	4.43	1.89	3.31
Qz norm	39.73	29.93	39.93	28.14	36.84	31.02	38.69	43.01	37.99	40.32	40.33	34.53	40.99	32.80	36.75	4.48	25.86
Crn norm	4.61	2.86	5.85	3.65	4.34	3.64	2.57	4.07	2.89	2.98	5.52	4.18	4.50	3.78	3.96	0.94	1.07
Or norm	39.50	51.44	39.15	51.17	39.97	46.31	45.12	39.64	43.86	40.31	32.93	44.83	43.53	52.96	43.60	5.40	52.98
Ab norm	10.95	8.21	8.58	9.19	11.47	12.22	8.76	8.52	9.26	11.36	14.07	6.41	5.52	5.36	9.27	2.45	15.12
An norm	1.76	2.19	2.19	2.23	2.90	1.63	1.89	1.91	3.01	2.08	3.01	2.55	1.81	1.54	2.19	0.48	3.28
Density	2.48	2.47	2.51	2.51	2.42	2.43	2.41	2.51	2.43	2.48	2.50	2.50	2.49	2.44	2.47	0.03	2.30
Viscosity(S96)	$10^{4.8}$	$10^{4.5}$	$10^{5.0}$	$10^{4.9}$	$10^{4.0}$	$10^{4.1}$	$10^{4.1}$	$10^{5.2}$	$10^{4.3}$	$10^{4.9}$	$10^{4.9}$	$10^{4.8}$	$10^{4.9}$	$10^{4.2}$	$10^{4.6}$	$10^{0.4}$	$10^{3.8}$
Viscosity(G08)	$10^{5.3}$	$10^{4.5}$	$10^{5.6}$	$10^{5.0}$	$10^{4.1}$	$10^{4.1}$	$10^{4.4}$	$10^{6.1}$	$10^{4.6}$	$10^{5.5}$	$10^{5.4}$	$10^{4.9}$	$10^{5.4}$	$10^{4.4}$	$10^{4.9}$	$10^{0.6}$	$10^{3.7}$

ASI values are calculated on anhydrous basis. S96, Scaillet *et al.* (1996); G08, Giordano *et al.* (2008).
PEM, melt compositions calculated by phase equilibria modeling at 950 °C with 25 mol% melts reintegrated back into bulk rock compositions.

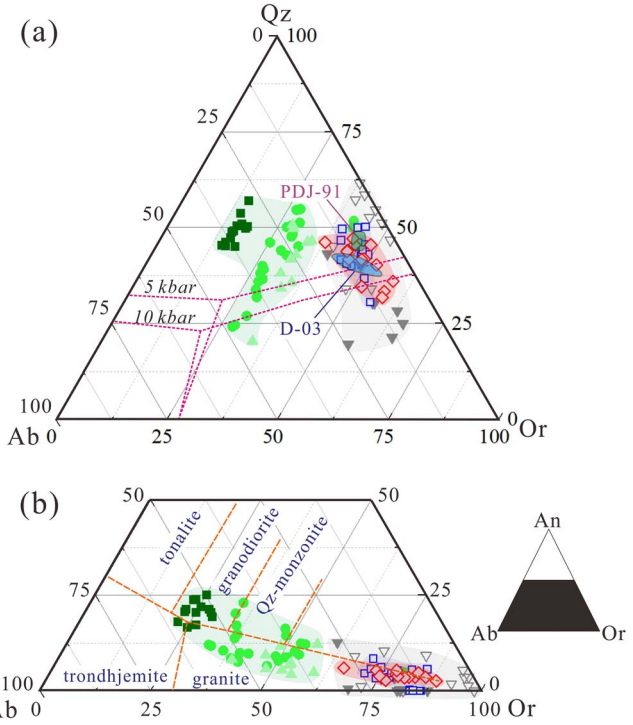

Fig. 10. (a) CIPW Qz–Ab–Or diagram showing normative compositions of analyzed NIs (normalized to 100% on anhydrous basis). Pink dashed lines show the eutectic points and cotectic lines for the subaluminous haplogranite system at $a_{H2O} = 1$ and different pressures (Luth *et al.*, 1964). References to experimental glasses: PDJ91 (shown in green), 950°C and 7 kbar (Patiño Douce & Johnston, 1991); D03 (shown in blue), 900°C and 5 kbar (Droop *et al.*, 2003). (b) An–Or–Ab diagram showing the normative compositions of analyzed NIs (after O'Connor, 1965). For the symbols, please refer to Fig. 9.

Peak and post–peak evolution of the Mather *UHT* metapelitic granulites

A pseudosection for the rocks was constructed within a *P–T* window of 3–15 kbar and 750–1200°C. Due to lower diffusion rates of Al^{3+} compared to Fe^{2+} and Mg^{2+}, aluminum contents in orthopyroxene are considered reliable to document the peak temperatures of *UHT* metamorphism. As shown in Fig. 13a, the pseudosection is contoured by (X_{Mg}(Opx) = Mg/(Fe^{2+} + Mg)) and y_{Al}(Opx) in order to retrieve peak *P–T* conditions. The interpreted peak assemblage of garnet + orthopyroxene + biotite + melt is stable over a wide P–T range (>7.5 kbar and > 860°C). The measured highest y_{Al} (0.18–0.19) and X_{Mg} (0.775–0.780) in orthopyroxene intersect at 12–13 kbar and 1070–1130°C, which is interpreted as the peak *P–T* conditions.

The peak minerals usually show breakdown to intergrowths of orthopyroxene$_2$ + cordierite ± biotite ± plagioclase ± spinel or sapphirine + cordierite at the post–peak stage. As shown in the enlarged P–T diagram (P = 5.0–9.0 kbar and T = 800–1000°C) (Fig. 13b), these assemblages occupy a narrow field, constraining the *P–T* conditions to 6.5–7.0 kbar and 910–950°C (outlined by purple bold lines). Plagioclase from the orthopyroxene–cordierite–bearing intergrowths has a typical X_{An} of 0.80–0.81, consistent with the prediction by the modeling. The inferred final assemblage is featured by later growth of sapphirine, biotite and plagioclase, which is predicted to be stable at a narrow pressure range of 6.5–6.8 kbar, with temperatures varying from 825 to 900°C. This field is bounded by the fluid-absent solidus, rutile-in, garnet- and ilmenite-out curves. The measured X_{Mg} in biotite (~0.81) and X_{An} in plagioclase (0.51–0.58) are consistent with the P–T field, further constraining the cooling path through *P–T* conditions of 6.5–7.0 kbar and 830–870°C (outlined by black bold lines).

Tracking the pre-peak melting process with melt reintegration

Phase equilibria modeling suggests that the solidus is located between 800 and 870°C (at 3–7 kbar) and the rock produces <15 vol.% melt at the peak stage, which is much lower than the expected values for metapelites. In addition, biotite is predicted to be stable at >1100°C (Fig. 13a). All these observations are in agreement with the strongly residual character of the bulk rock composition (SiO_2 = 44 wt.%). Thus, this composition obtained from XRF analysis is only appropriate for modeling the peak and post-peak metamorphic evolutions (White *et al.*, 2004; Liu *et al.*, 2020). Here we explore the potential effects of melt loss on the topology during pre-peak evolution by reintegrating a certain amount of melts to the residual composition (Bartoli, 2017, 2019). The simplified chemical systems with respect to natural occurrences (Bartoli & Carvalho, 2021) and the limitations of solution models (White *et al.*, 2011) make it impossible to precisely predict the primary melt compositions of partially melted rocks. As a consequence, NIs are used as proxy of the pristine melts that was present in the system (e.g. Bartoli, 2019). This single-step melt reintegration may be only suitable to reconstruct the probable bulk rock compositions (BRC) at or near *UHT* conditions as the rock may have undergone several episodes of melt loss (e.g. White *et al.*, 2014; Bartoli, 2017) and the compositions of NIs cannot represent the melt compositions generated at low temperatures.

The presence of trapped rutile grains within NIs are confirmed by Raman analyses (Fig. 5g), but not observed in the matrix or predicted by the phase equilibria modeling (Fig. 13). As shown in Fig. 14a, rutile is expected to appear at >950°C if >20 mol.% melts are reintegrated back into the rock. This is consistent with their presence as trapped phase within the NIs (Fig. 5g), and is strongly supportive of the entrapment of rutile–bearing melt inclusions at *UHT* conditions. With 25 mol.% melts reintegrated back into the BRC, the modeling predicts that most melts (~40 mol.%) were produced in the temperature range of 850–950°C. The melt reintegration also results in a reduction of the stability field of biotite, which is predicted to disappear at >950°C (Fig. 14a). The melt composition calculated at 12.5 kbar and 950°C shows slightly higher Na_2O and K_2O contents (Table 3). This divergence between NIs and the calculated melts was also documented in other case studies, and was ascribed to the lack of equilibrium with the residuum or diffusion in the melts, and alternatively, the imperfections of forward phase equilibria modeling (Bartoli & Carvalho, 2021).

The *P–T* pseudosection reconstructed with a reintegration of 25 mol.% melts into the BRC is shown in Fig. 14b. The most evident changes are expansions of the stability fields of K – feldspar and rutile, which were predicted to be stable during prograde melting. Despite the fact that kyanite/sillimanite is absent in the investigated rocks, kyanite pseudomorphs (Tong & Wilson, 2006) and kyanite relics replaced by sapphirine + quartz (Harley, 2021) have been identified in rocks from the same region, suggesting that the rocks may have been in the kyanite stability field. The quartz–, kyanite–in and plagioclase–out curves suggest that the rocks underwent a nearly isobaric heating from M0 to M1 stage (shown by dashed lines in Fig. 13a). Accordingly, the Mather *UHT* granulites may have experienced a clockwise *P–T* path with peak conditions of 12–13 kbar and 1070–1130°C,

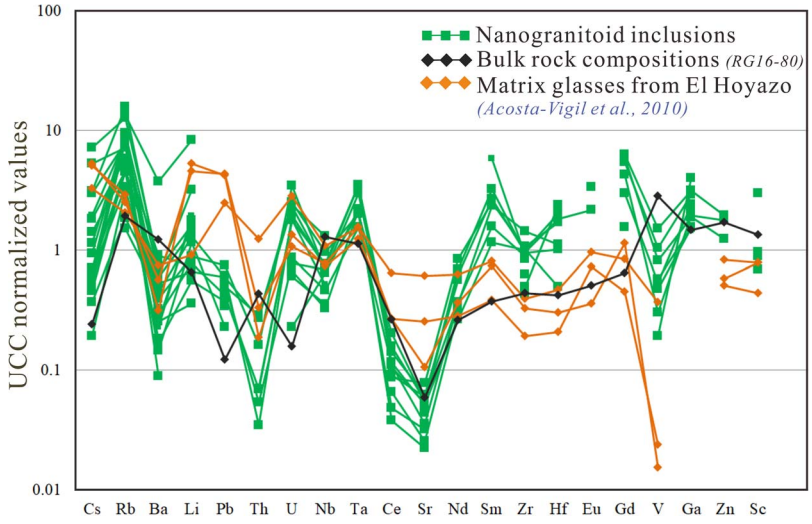

Fig. 11. Trace element compositions of NIs and granulitic restite, normalized to the average upper continental crust (UCC) composition (data from Rudnick & Gao, 2014). Trace elements of matrix glasses within metapelitic enclaves from El Hoyazo (SE Spain) (samples HO−50A, −33A and − 54; Acosta Vigil *et al.*, 2010) are also shown for comparison. Note that peak *P–T* conditions for the metapelitic enclaves from El Hoyazo are 850 ± 50°C and 5–7 kbar, slightly lower than the investigated rocks in this study.

followed by decompression and cooling to 6.5–7.0 kbar and 910–950°C, and finally isobaric cooling (IBC) to solidus conditions (P = 6.5–7.0 kbar; T = 830–870°C).

DISCUSSIONS

P–T conditions of melt entrapment and anatectic regime

In East Antarctica, NIs in high–grade metamorphic rocks have been reported from the Lützow–Holm Complex (Spr-bearing *UHT* metapelitic granulites; Carvalho *et al.*, 2023a), the Dronning Maud Land (ultramafic granulites; Ferrero *et al.*, 2018), the Northern Victoria Land (metagreywackes; Ferri *et al.*, 2020), and the Sør Rondane Mountains (East Antarctica) (Sil–Grt–Bt gneiss; Higashino & Kawakami, 2022). The present study expands the existing database to include the melts produced by *UHT* metamorphism of the Mg-rich and Sil-absent metapelitic rocks from the Rauer Islands.

The presence of kokchetavite and kumdykolite is confirmed by Raman analyses (Fig. 5g). Kokchetavite has been found within multiphase inclusions in high to ultrahigh pressure (*HP–UHP*) rocks, which was considered to crystalize from K-rich melts and may exist as a metastable phase (e.g. Hwang *et al.*, 2004, 2013; Ferrero *et al.*, 2016; Borghini *et al.*, 2018, 2023; Gao & Liu, 2018). Kumdykolite was not only present as inclusions within *HP–UHP* rocks (e.g. Hwang *et al.*, 2009; Kotková *et al.*, 2014; Ferrero *et al.*, 2016; Borghini *et al.*, 2018, 2023; Gao & Liu, 2018), but also found in chondrites (Németh *et al.*, 2013). However, Ferrero *et al.* (2016) concluded that high pressure is not required for the formation of kumdykolite and kokchetavite, and their presence is thus not an indicator of *UHP* conditions. More recently, NIs from granulites have also been reported to preserve kokchetavite and/or kumdykolite as daughter phases (Ferrero & Angel, 2018; Carvalho *et al.*, 2019; Gianola *et al.*, 2021). Therefore, both kokchetavite and kumdykolite may have crystalized from *HT* to *UHT* melts, and cannot be used to infer the *P–T* entrapment conditions. According to Ferrero *et al.* (2016), the presence of feldspar polymorphs indicates that the melt compositions (in terms of major elements and volatiles) are mostly preserved.

Melting during heating is predicted by phase equilibria modeling (Figs 13 and 14). Rutile is present within NIs as an accidentally trapped phase (Fig. 5g). However, it is not observed in the matrix of the rocks. This suggests that rutile existed in the pre – peak stage and became metastable as a consequence of melt extraction and loss. After an integration of ~25% melts into the granulitic restite, phase equilibria modeling predicts that rutile appears when temperature exceeds 950°C at 12.5 kbar (Fig. 14), highly in agreement with the remelting experimental constraints given by NIs at 12.5 kbar. Furthermore, some NIs occur near to high−Al orthopyroxene inclusions (Al_2O_3 = 8.85–9.04 wt.%) within garnets (Fig. 3a). These are strong evidence that at least some NIs investigated in this study were trapped at *UHT* conditions. Although the rocks studied here have undergone peak temperatures of 1070–1130°C, the melts may be produced at or near *UHT* conditions (850–950°C).

The H_2O contents of NIs show variable values ranging from 1.49 to 4.24 wt.% (Table 3), suggestive of heterogeneous distributions of water (Bartoli *et al.*, 2014) or existences of C-bearing phases in some NIs (e.g. Carvalho *et al.*, 2019; Ferri *et al.*, 2020; Gianola *et al.*, 2021). Estimation of H_2O by difference of EMPA totals from 100% usually overestimates the H_2O contents of NIs (e.g. Cesare *et al.*, 2015), and specific reasons for this inconsistency still need further investigations. As shown in Figs 9 and 10, the highly silicic, peraluminous and potassic to ultrapotassic NIs have also been found in peritectic garnets from the Kerala Khondalite Belt (Cesare *et al.*, 2009; Ferrero *et al.*, 2012), the Gruf Complex (Gianola *et al.*, 2021) and the Lützow–Holm Complex (Carvalho *et al.*, 2023a). Moreover, K-rich melts have also been experimentally derived from pelitic starting materials under *UHT* conditions (e.g. Droop *et al.*, 2003; Patiño–Douce & Johnston, 1991). Ti and Fe^{3+} are expected to stabilize biotite to expand the Bt-dehydration melting to occur at higher temperatures (e.g. White *et al.*, 2014), which likely accounts for the enrichments of K_2O in *HT* to *UHT* melts (Gianola *et al.*, 2021). However, it is also evident that melt compositions of *HT–UHT* granulites from the Ivrea Zone plot away from the K – apex of the triangle (Fig. 10), with low K_2O contents of ~2.0 wt.% (Carvalho *et al.*, 2019). The authors argued that the low-K melts may be produced at *P–T* conditions approaching the Bt-out curves

Table 4: Trace element concentrations of NIs and the granulitic restite from the Mather Peninsula. The trace element compositions are shown in ppm

	80_05	80_07	80_09	80_10	80_12	80_16	80_18	80_21	80_24	80_25	80_27	80_38	80_48	80_03*	80_08*	80_26*	80_13*	80_44*	80_46*	80_47*	80_42*	80_11*	ave.	σ	WRC
Rb	268.8	755.9	387.1	708.9	711.7	676.6	732.7	282.3	385.7	212.2	156.6	126.7	605.0	411.1	798.8	1131.7	1325.0	380.3	489.2	1077.4	402.1	691.9	578.1	312.9	162.4
Cs	0.9	5.6	2.6	9.5	2.8	14.7	4.6	3.2	6.9	1.8	1.8	b.d.l.	26.1	2.3	3.3	b.d.l.	15.3	3.4	9.0	35.5	3.5	2.9	7.8	8.8	1.2
Ba	180.2	203.0	107.6	143.3	279.7	56.3	162.3	114.7	91.1	446.7	332.1	267.5	248.2	159.7	398.3	2364.7	432.8	402.3	565.6	483.7	373.7	275.1	367.7	457.2	769.5
Li	18.8	b.d.l.	13.5	46.5	31.5	b.d.l.	42.7	b.d.l.	27.8	b.d.l.	16.0	b.d.l.	21.5	8.6	76.9	200.8	38.8	b.d.l.	17.8	b.d.l.	33.9	b.d.l.	42.5	47.0	15.6
Pb	7.2	10.4	6.3	b.d.l.	10.1	5.8	b.d.l.	8.9	3.9	9.9	10.1	8.6	12.8	*n.c*	*n.c*	*n.c*	*n.c*	*n.c*	*n.c*	*n.c*	*n.c*	*n.c*	8.5	2.4	2.1
Th	0.7	0.4	b.d.l.	0.8	b.d.l.	b.d.l.	b.d.l.	0.6	b.d.l.	3.8	2.8	3.0	1.7	*n.c*	*n.c*	*n.c*	*n.c*	*n.c*	*n.c*	*n.c*	*n.c*	*n.c*	1.7	1.2	4.5
U	4.8	5.2	2.3	4.9	6.4	1.6	0.6	2.1	1.8	8.7	6.3	6.8	9.3	*n.c*	*n.c*	*n.c*	*n.c*	*n.c*	*n.c*	*n.c*	*n.c*	*n.c*	4.7	2.7	0.4
Nb	9.3	8.7	5.6	6.2	15.7	4.2	7.8	8.4	4.0	14.3	8.4	11.6	8.0	*n.c*	*n.c*	*n.c*	*n.c*	*n.c*	*n.c*	*n.c*	*n.c*	*n.c*	8.6	3.4	15.4
Ta	3.2	3.2	1.4	b.d.l.	b.d.l.	b.d.l.	2.0	1.8	2.0	3.2	b.d.l.	1.8	2.7	*n.c*	*n.c*	*n.c*	*n.c*	*n.c*	*n.c*	*n.c*	*n.c*	*n.c*	2.4	0.7	1.0
Ti	997.5	1052.6	793.0	963.1	904.3	334.2	419.1	470.5	274.1	734.6	654.5	705.3	314.5	*n.c*	*n.c*	*n.c*	*n.c*	*n.c*	*n.c*	*n.c*	*n.c*	*n.c*	662.9	265.1	*n.c*
Ce	7.3	10.0	7.0	6.7	5.5	4.1	b.d.l.	3.0	2.4	13.4	5.8	12.8	8.9	*n.c*	*n.c*	*n.c*	*n.c*	*n.c*	*n.c*	*n.c*	*n.c*	*n.c*	7.2	3.4	16.8
Sr	16.6	17.8	11.4	17.0	24.8	8.2	14.1	10.2	7.2	27.6	19.0	17.9	20.0	*n.c*	*n.c*	*n.c*	*n.c*	*n.c*	*n.c*	*n.c*	*n.c*	*n.c*	16.3	5.8	19.0
Nd	7.2	16.7	10.0	b.d.l.	22.8	8.3	b.d.l.	b.d.l.	b.d.l.	16.8	9.7	18.7	15.2	*n.c*	*n.c*	*n.c*	*n.c*	*n.c*	*n.c*	*n.c*	*n.c*	*n.c*	13.9	5.0	7.1
Sm	5.5	12.6	7.4	27.2	11.8	b.d.l.	b.d.l.	b.d.l.	b.d.l.	19.0	11.1	15.3	b.d.l.	*n.c*	*n.c*	*n.c*	*n.c*	*n.c*	*n.c*	*n.c*	*n.c*	*n.c*	13.7	6.4	1.8
Zr	194.9	185.1	172.9	173.9	197.0	84.2	206.3	163.8	121.1	256.0	276.5	182.8	96.2	*n.c*	*n.c*	*n.c*	*n.c*	*n.c*	*n.c*	*n.c*	*n.c*	*n.c*	177.8	47.7	84.9
Hf	10.7	9.7	b.d.l.	b.d.l.	2.6	b.d.l.	9.0	b.d.l.	b.d.l.	12.5	5.9	5.4	12.7	*n.c*	*n.c*	*n.c*	*n.c*	*n.c*	*n.c*	*n.c*	*n.c*	*n.c*	8.6	3.4	2.2
Eu	b.d.l.	2.2	b.d.l.	b.d.l.	b.d.l.	b.d.l.	b.d.l.	b.d.l.	3.4	b.d.l.	b.d.l.	b.d.l.	b.d.l.	*n.c*	*n.c*	*n.c*	*n.c*	*n.c*	*n.c*	*n.c*	*n.c*	*n.c*	2.8	0.6	0.5
Gd	6.3	b.d.l.	11.9	b.d.l.	b.d.l.	17.1	b.d.l.	21.9	b.d.l.	b.d.l.	b.d.l.	23.9	25.1	*n.c*	*n.c*	*n.c*	*n.c*	*n.c*	*n.c*	*n.c*	*n.c*	*n.c*	17.7	6.8	2.6
V	b.d.l.	b.d.l.	52.0	b.d.l.	b.d.l.	29.4	18.6	101.1	55.5	35.8	46.1	79.7	146.6	*n.c*	*n.c*	*n.c*	*n.c*	*n.c*	*n.c*	*n.c*	*n.c*	*n.c*	62.7	38.1	274.7
Ga	b.d.l.	33.2	42.4	25.7	35.7	34.3	70.5	50.7	27.1	18.8	26.9	32.8	55.3	*n.c*	*n.c*	*n.c*	*n.c*	*n.c*	*n.c*	*n.c*	*n.c*	*n.c*	37.8	14.0	25.9
Zn	b.d.l.	83.3	b.d.l.	b.d.l.	b.d.l.	119.8	b.d.l.	b.d.l.	b.d.l.	b.d.l.	b.d.l.	b.d.l.	130.7	*n.c*	*n.c*	*n.c*	*n.c*	*n.c*	*n.c*	*n.c*	*n.c*	*n.c*	111.2	20.3	114.9
Sc	b.d.l.	b.d.l.	12.4	b.d.l.	b.d.l.	b.d.l.	b.d.l.	42.0	b.d.l.	b.d.l.	9.7	13.5	b.d.l.	*n.c*	*n.c*	*n.c*	*n.c*	*n.c*	*n.c*	*n.c*	*n.c*	*n.c*	19.4	13.1	19.0
Trapped phases														Apt	Mnz	Apt; Zrn	Mnz	Rt	Rt; Mnz	Rt	Rt	Rt			
Rb/Sr	16.21	42.48	33.93	41.79	28.65	82.46	52.08	27.74	53.71	7.69	8.22	7.08	30.25										33.3	20.9	8.56
Sm/Nd	0.76	0.76	0.74		0.52					1.13	1.14	0.82											0.8	0.2	0.25
U/Th	6.62	14.47		6.39				3.74		2.27	2.22	2.27	5.47										5.4	3.8	0.09

b.d.l. below detection limit; *n.c* not considered; WRC, whole-rock composition; ∗ Nanogranitoid inclusions with accidentally trapped phases such as zircon, monazite, apatite and rutile.

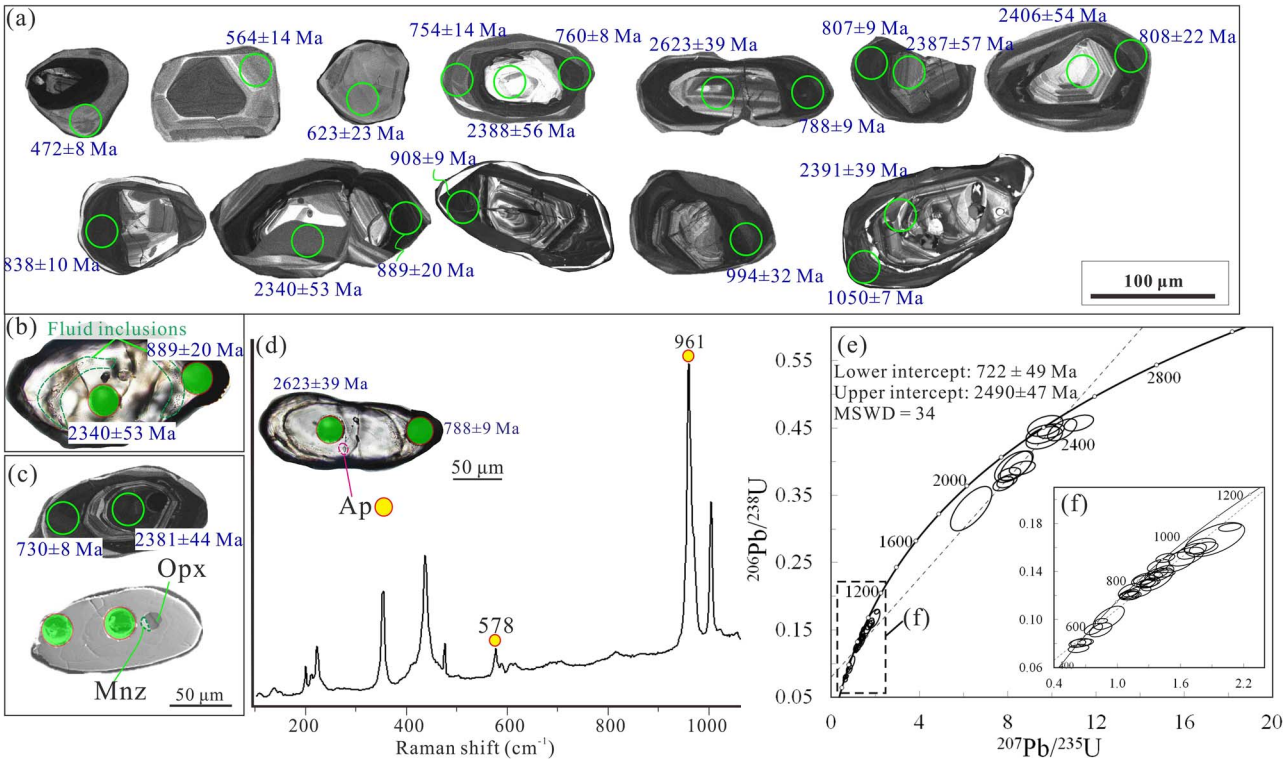

Fig. 12. (a) CL images of representative zircons mounted on epoxy resins. Green circles represent analyzed spots and the nearby blue numbers represent their isotopic dates. (b–d) Photographs showing inclusions within zircons. (e) Concordia diagram showing the results of U–Pb zircon dating. (f) Enlarged concordia diagram of the box in (e).

(Carvalho *et al.*, 2019). Alternatively, participation of plagioclase in the prograde melting reactions may also be responsible for the relatively higher CaO/NaO concentrations in that study. The potassic nature of melts, coupled with phase equilibria modeling (Fig. 14), supports that the melts were produced by Bt-dehydration melting of pelites under *HT* to *UHT* conditions (850–950°C).

Our data show that the melts are enriched in Li, Cs, Rb, Ta, Sm, Nd, Zr, U and Pb and depleted in Ce, Th, Ba, Sr and Nb relative to the granulitic restite (Table 4; Fig. 11). Dissolution of zircon or monazite during high temperature melting (Kelsey & Powell, 2011) may contribute to the U, Pb and Zr enrichments in anatectic melts. NIs in this study are depleted in Ce (<12.8 ppm) and Th (<3.8 ppm), which may be ascribed to the shielding of some monazites by porphyroblastic phases (Huang *et al.*, 2021) or disequilibrium melting (Watt & Harley, 1993). It suggests that the melts are likely undersaturated with respect to monazite. Besides, the melts show mild depletion of Ba compared with the restite. K – feldspar is the most important repository of Ba in the rocks and it was still stable during melting, which might reserve appreciable amounts of Ba (Zeng *et al.*, 2005).

The investigated melts contain higher Rb contents than the melts produced through Ms – dehydration melting (Acosta Vigil *et al.*, 2010, 2012; Bartoli *et al.*, 2019), consistent with melts yielded by Bt – dehydration melting because biotite is the major reservoir of Rb (e.g. Acosta Vigil *et al.*, 2010; Wolf *et al.*, 2019). They also show higher Rb contents relative to the matrix glasses from El Hoyazo (Fig. 11), which were considered to be yielded at the onset of biotite–dehydration melting (Acosta Vigil *et al.*, 2010). Moreover, Sr contents are usually low in micas but abundant in plagioclase (Weinberg & Hasalová, 2015), and plagioclase was not involved in the incongruent melting in this study. Thus, higher Rb/Sr ratios of the investigated NIs can be attributed to Bt – dehydration melting in the absence of plagioclase. On the other hand, although Zeng *et al.* (2005) previously pointed out that that Ms/Bt – dehydration melting and dissolution of apatite will produce melts with high Sm/Nd values, the mechanisms that caused elevated Sm/Nd ratios in the melts are still vague. Assuming no isotopic fractionations of Nd and Sr, enrichments of Sm and Rb in anatectic melts are expected to result in higher $^{143}Nd/^{144}Nd$ and $^{87}Sr/^{86}Sr$ values in melts than the granulitic restite after enough long time.

Physical properties of the hottest crustal melts

The chemical data of NIs allow to peer into physical properties of the melts and therefore, may provide insights into rheology and mobility of the hottest granitic melts and their potential effects on orogenic evolution. Assuming conditions of $P = 12$ kbar and $T = 950$°C, the average compositions of re-homogenized melt inclusions are considered to have densities of 2.47 ± 0.07 g/cm^3, calculated with program DensityX (Iacovino & Till, 2019). These values are slightly higher than previously estimated densities for hydrous granitic melts (~2.20 g/cm^3; Clemens & Vielzeuf, 1987), but lower than the average density for granites (~2.70 g/cm^3; Artemieva *et al.*, 2017).

Viscosity of melts may be affected by several potential factors, such as fluid contents (Scaillet *et al.*, 1996; Holtz *et al.*, 2001) and melt compositions (Giordano *et al.*, 2008). At 950°C, applications of the equations of Giordano *et al.* (2008) and Scaillet *et al.* (1996) yield melt viscosities of $10^{4.1}$–$10^{6.1}$ Pa·s and $10^{4.0}$–$10^{5.2}$ for the investigated melts, respectively. When considering the average melt compositions, these methods produce results of $10^{4.9 \pm 1.2}$ and $10^{4.6 \pm 0.8}$ Pa·s. As the estimated H_2O contents for the melts based on difference of EMPA totals from 100% usually slightly

Table 5: LA – ICP – MS analysis results for zircons from the Mather *UHT* granulites

Spot	Th (ppm)	U (ppm)	Th/U	$^{206}Pb/^{238}U$	1σ	$^{207}Pb/^{206}Pb$	1σ	$^{207}Pb/^{235}U$	1σ	$^{206}Pb/^{238}U$ (Ma)	1σ	$^{207}Pb/^{206}Pb$ (Ma)	1σ	$^{207}Pb/^{235}U$ (Ma)	1σ
Rim															
1	49	145	0.34	0.076	0.001	0.060	0.004	0.633	0.040	472	8	611	157	498	25
2	45	167	0.27	0.080	0.001	0.057	0.003	0.621	0.033	497	8	480	120	490	20
3	40	143	0.28	0.081	0.001	0.059	0.004	0.656	0.040	500	9	565	136	512	25
4	98	437	0.22	0.081	0.001	0.062	0.003	0.699	0.030	502	7	676	96	538	18
5	47	420	0.11	0.091	0.002	0.065	0.003	0.842	0.044	564	14	770	96	620	24
6	57	271	0.21	0.092	0.002	0.061	0.003	0.774	0.035	569	11	657	100	582	20
Mantle															
7	8	877	0.01	0.099	0.001	0.062	0.002	0.848	0.024	607	5	661	66	624	13
8	23	481	0.05	0.101	0.004	0.062	0.003	0.920	0.060	623	23	687	95	662	32
9	18	1126	0.02	0.120	0.001	0.068	0.002	1.136	0.037	730	8	865	65	771	18
10	32	659	0.05	0.120	0.001	0.067	0.002	1.115	0.039	730	8	843	70	761	18
11	18	811	0.02	0.121	0.001	0.066	0.002	1.110	0.037	735	8	1200	71	758	18
12	22	1024	0.02	0.122	0.001	0.066	0.002	1.123	0.031	743	7	817	59	765	15
13	48	524	0.09	0.123	0.002	0.070	0.002	1.210	0.045	750	11	937	67	805	21
14	42	521	0.08	0.124	0.002	0.065	0.002	1.115	0.043	754	14	759	70	760	21
15	31	1178	0.03	0.130	0.002	0.072	0.002	1.301	0.035	788	9	983	55	846	16
16	21	955	0.02	0.130	0.002	0.070	0.002	1.273	0.036	788	9	943	54	834	16
17	42	848	0.05	0.131	0.002	0.072	0.002	1.310	0.040	793	9	981	56	850	17
18	15	821	0.02	0.133	0.002	0.067	0.002	1.245	0.045	806	13	835	61	821	20
19	12	675	0.02	0.133	0.002	0.068	0.002	1.257	0.043	807	9	861	72	827	19
20	43	666	0.06	0.133	0.004	0.073	0.003	1.376	0.063	808	22	1013	70	879	27
21	14	1386	0.01	0.136	0.001	0.071	0.002	1.345	0.035	822	8	955	49	865	15
22	22	825	0.03	0.138	0.001	0.076	0.002	1.448	0.041	836	7	1087	55	909	17
23	10	548	0.02	0.139	0.003	0.073	0.002	1.421	0.047	837	15	1020	54	898	20
24	21	765	0.03	0.139	0.002	0.072	0.002	1.384	0.040	838	10	977	61	882	17
25	24	1183	0.02	0.145	0.002	0.069	0.002	1.391	0.043	873	12	889	57	885	18
26	47	758	0.06	0.148	0.004	0.073	0.002	1.552	0.074	889	20	1013	67	951	30
27	10	1346	0.01	0.151	0.002	0.069	0.002	1.456	0.037	908	9	898	56	912	15
28	20	1432	0.01	0.152	0.003	0.076	0.002	1.654	0.069	915	18	1098	57	991	26
29	23	944	0.02	0.157	0.003	0.078	0.002	1.708	0.056	940	15	1139	57	1012	21
30	26	972	0.03	0.160	0.002	0.081	0.002	1.820	0.055	954	12	1232	56	1053	20
31	27	805	0.03	0.161	0.003	0.078	0.002	1.783	0.062	964	15	1158	55	1039	22
32	19	707	0.03	0.167	0.006	0.078	0.003	1.924	0.116	994	32	1154	64	1090	40
33	21	1131	0.02	0.177	0.001	0.084	0.002	2.069	0.044	1050	7	1292	40	1139	14
Core															
34	151	529	0.28	0.330	0.013	0.129	0.004	6.343	0.383	1840	65	2088	56	2024	53
35	172	219	0.79	0.393	0.009	0.150	0.005	8.258	0.349	2135	44	2340	53	2260	38
36	242	351	0.69	0.394	0.009	0.151	0.004	8.407	0.306	2140	42	2361	48	2276	33
37	58	289	0.20	0.367	0.004	0.152	0.004	7.803	0.193	2017	20	2374	41	2209	22
38	101	144	0.70	0.382	0.004	0.153	0.004	8.080	0.210	2085	18	2381	44	2240	24
39	140	167	0.83	0.453	0.006	0.154	0.005	9.704	0.327	2410	28	2387	57	2407	31
40	216	378	0.57	0.371	0.004	0.154	0.004	7.970	0.188	2035	19	2391	39	2228	21
41	80	140	0.57	0.441	0.006	0.155	0.005	9.582	0.307	2355	26	2406	54	2395	30
42	798	441	1.81	0.391	0.004	0.160	0.004	8.661	0.241	2126	19	2452	46	2303	25
43	233	337	0.69	0.446	0.004	0.160	0.004	9.951	0.249	2376	20	2461	41	2430	23
44	50	49	1.01	0.436	0.007	0.161	0.006	9.656	0.338	2331	31	2465	58	2403	32
45	138	234	0.59	0.448	0.007	0.168	0.004	10.468	0.270	2384	30	2540	38	2477	24
46	118	227	0.52	0.458	0.005	0.177	0.004	11.225	0.273	2429	22	2623	39	2542	23

higher than their real values due to the possible presence of CO_2 (e.g. Cesare *et al.*, 2015), the calculated viscosities may represent the minimum values. Viscosities for the investigated melts are roughly in agreement with the calculation results for melt inclusions within *UHT* granulites from the Gruf Complex ($10^{4.1}$–$10^{4.8}$ Pa·s; Gianola *et al.*, 2021). These values also overlap the estimates of granitic melts that were experimentally derived at 5–8 kbar and 700–950°C ($10^{4.3}$–$10^{5.4}$ Pa·s) (Hess & Dingwell, 1996; Scaillet *et al.*, 1996). However, melts formed at low temperature (~700°C) showed higher viscosities (~$10^{6.0}$ Pa·s) (Bartoli *et al.*, 2013b), and therefore less mobile and result in slower rates of melt segregation and ascent (Holtz *et al.*, 2001; Brown, 2013; Bartoli *et al.*, 2013b). Clemens *et al.* (2020) concluded that melting at high temperatures (mostly >850°C) under fluid-deficient or -absent conditions are usually highly mobile, and therefore, the low viscosity melts may facilitate melt extraction, and consequently crustal differentiation and redistribution of heat–producing elements (such as K, Th and U) (Gianola *et al.*, 2021).

The melts are enriched in heat producing elements such as K and U. Despite that the melts are depleted in Th, the heat production rate of Th (0.072 $\mu W/m^3$) is much lower than that of U (0.265 $\mu W/m^3$) (Bea, 2012). The capacity for heat production

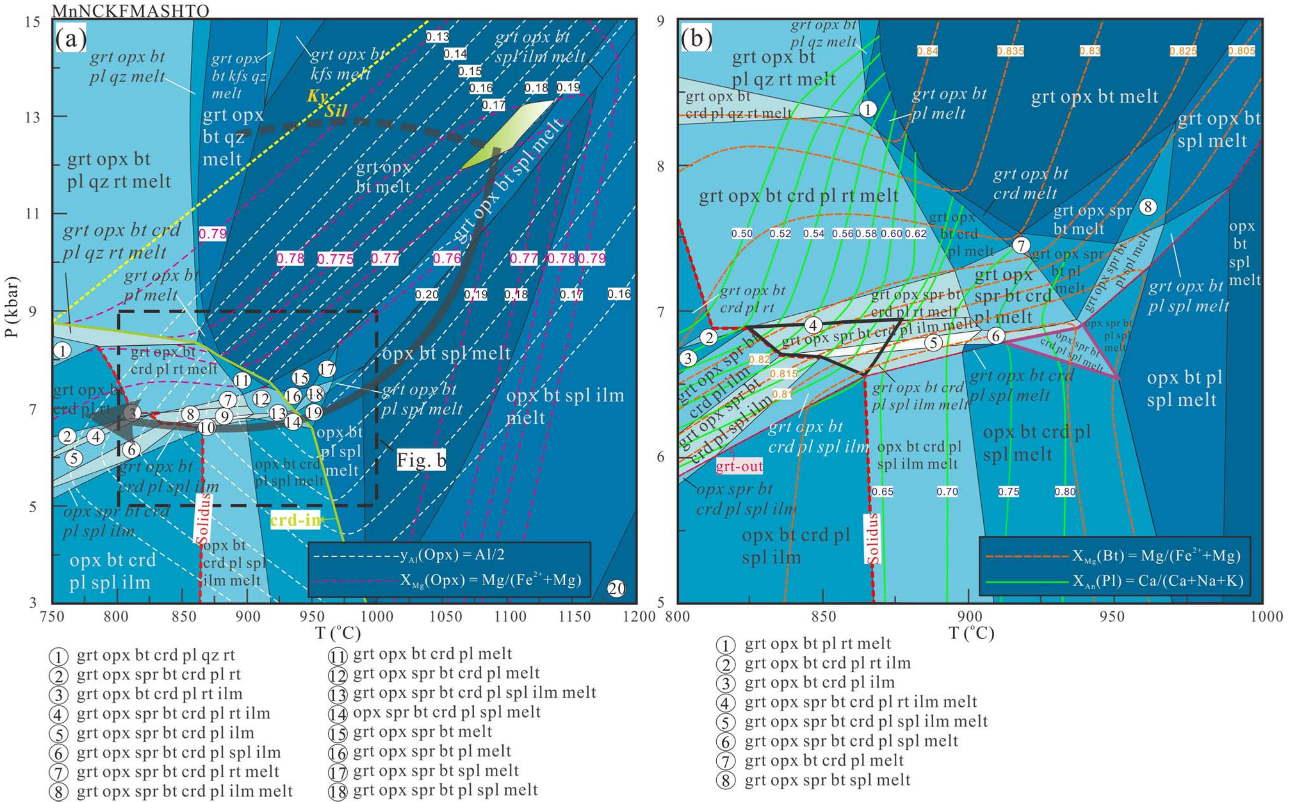

① grt opx bt crd pl qz rt
② grt opx spr bt crd pl rt
③ grt opx bt crd pl rt ilm
④ grt opx spr bt crd pl rt ilm
⑤ grt opx spr bt crd pl ilm
⑥ grt opx spr bt crd pl spl ilm
⑦ grt opx spr bt crd pl rt melt
⑧ grt opx spr bt crd pl ilm melt
⑨ grt opx spr bt crd pl spl ilm melt
⑩ grt opx bt crd pl spl ilm melt
⑪ grt opx bt crd pl melt
⑫ grt opx spr bt crd pl melt
⑬ grt opx spr bt crd pl spl ilm melt
⑭ opx spr bt crd pl spl melt
⑮ grt opx spr bt melt
⑯ grt opx spr bt pl melt
⑰ grt opx spr bt spl melt
⑱ grt opx spr bt pl spl melt
⑲ opx spr bt pl spl melt
⑳ opx spl ilm melt

① grt opx bt pl rt melt
② grt opx bt crd pl rt ilm
③ grt opx bt crd pl ilm
④ grt opx spr bt crd pl rt ilm melt
⑤ grt opx spr bt crd pl spl ilm melt
⑥ grt opx spr bt crd pl spl melt
⑦ grt opx bt crd pl melt
⑧ grt opx spr bt spl melt

Bulk rock compositions:

MnO	Na_2O	CaO	K_2O	FeO	MgO	Al_2O_3	SiO_2	H_2O	TiO_2	O_2
0.06	0.24	0.51	2.11	9.88	29.25	9.18	43.67	4.00	1.01	0.09

Fig. 13. (a) *P*–*T* pseudosection calculated at X(Fe_2O_3) = Fe^{3+}/Fe^T = 0.35, with a *P*–*T* range of 3–15 kbar and 750–1200°C. The fluid-absent solidus is shown in red dashed curves and the interpreted peak *P*–*T* conditions are shown in pale yellow. The grey curves in (a) represent the inferred *P*–*T* path. (b) Enlarged *P*–*T* pseudosection with a *P*–*T* range of 5–9 kbar and 800–1000°C. The constrained *P*–*T* fields for the M2 and M3 stage are outlined by purple and black bold lines, respectively.

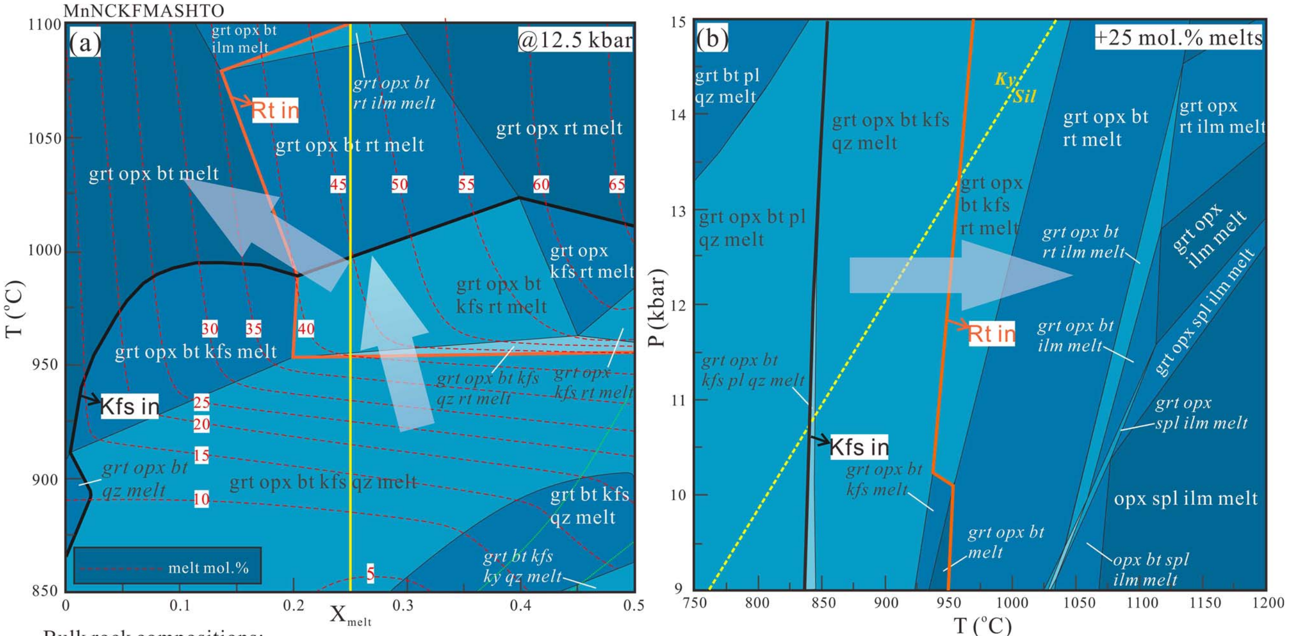

Bulk rock compositions:

	MnO	Na_2O	CaO	K_2O	FeO	MgO	Al_2O_3	SiO_2	H_2O	TiO_2	O_2
X_{melt}=0	0.06	0.24	0.51	2.11	9.88	29.25	9.18	43.67	4.00	1.01	0.09
X_{melt}=0.5	0.03	0.64	0.49	3.38	5.43	15.22	8.83	58.66	6.74	0.52	0.05

Bulk rock compositions:

MnO	Na_2O	CaO	K_2O	FeO	MgO	Al_2O_3	SiO_2	H_2O	TiO_2	O_2
0.05	0.44	0.50	2.75	7.65	22.23	9.01	51.17	5.37	0.76	0.07

Fig. 14. (a) $T - X_{melt}$ pseudosection showing the pre-peak evolution of the investigated rocks. Average re-homogenized nanogranitoid compositions are adopted as the melt compositions. The pressure is fixed at ~12.5 kbar. (b) Reconstructed *P*–*T* pseudosection after 25% melt reintegration into the bulk rock composition.

of the hot melts was determined with the following equation (Rybach, 1988):

$$H = \rho \times (0.0952 \times C_U + 0.0348 \times C_K + 0.0256 \times C_{Th}).$$

Where H is heat production in $\mu W/m^3$, ρ is density in g/cm^3, and C_U, C_K, and C_{Th} are concentrations of radioactive isotopes of U, K, and Th in ppm, wt.% and ppm, respectively.

As calculated above, the density of melts is estimated as 2.47 ± 0.07 g/cm^3. Calculated heat production value for the average melt composition is ~2.3 $\mu W/m^3$. However, the obtained K, U and Th contents of melts cannot represent their real concentrations during the thermal event because of long-standing decay of the parental elements. Accordingly, heat production of average melt compositions was back-calculated to ~530 Ma based on appropriate decay equations for ^{238}U, ^{235}U, ^{232}Th and ^{40}K. The resultant average value is ~2.8 $\mu W/m^3$, which is higher compared with bulk heat production in granitic rocks of all ages (~2.0 $\mu W/m^3$; Artemieva *et al.*, 2017).

Granitic melts investigated in this study are particularly rich in heat-producing elements (such as K and U), and show densities of 2.47 ± 0.07 g/cm^3 and viscosities of $10^{4.9 \pm 1.2}$ Pa•s. Such melts are mobile and prone to be extracted from the source, and as a consequence, might be responsible for the formation of large granitic intrusions. Stagnation and flow of such melts in the deep crust provides a potential source at the base of the crust to heat the orogenic hinterlands through radioactive decay of heat producing elements (Clark *et al.*, 2011; Gianola *et al.*, 2021), and may have a great influence on the thermal structure of the continental crust.

Secondary fluid infiltration and its implications for the timing of *UHT* metamorphism: Open questions

Fluid infiltration is a well–documented phenomenon in the Rauer Islands. For example, Harley (1998b) has suggested the growth of cordierites in Grt–Sil–Qz gneiss was linked with the ingress of CO_2-rich fluid ($X_{CO2} > 0.8$) based on secondary ion mass spectrometry analyses of H_2O and CO_2 in the secondary cordierite. On the contrary, coarser cordierites adjacent to leucosomes show lower X_{CO2} values of 0.05. Such features indicate that the fluid regime in this region has changed markedly as a consequence of ambient C–O–H fluid ingress. As zircon U–Pb systematics of the layered mafic complex and intrusive tonalites from the nearby Scherbinina Island show clear resetting at ~520 Ma, the fluid ingress was considered to have occurred at 530–510 Ma (Harley *et al.*, 1998; Harley & Kelly, 2007). On the other hand, Liu *et al.* (2021) reported that hornblende and clinopyroxene in mafic granulites from the Filla Island were partially replaced by actinolite, which was also ascribed by the authors to strong fluid activities during the Cambrian reworking. In this study, we report on the occurrence of multiphase fluid inclusions (i.e. magnesite, pyrophyllite, corundum and CO_2) within orthopyroxene and garnet (Fig. 7), which are considered to be secondary in origin. Such stepdaughter phases were previously recognized in garnet–hosted primary FIs (e.g. Tacchetto *et al.*, 2019; Carvalho *et al.*, 2020, 2023b; Gianola *et al.*, 2021). Here, we confirm that the secondary C – O – H fluid along the healed fractures of garnet and orthopyroxene at high temperatures could not survive neither, and has reacted with its hosts to produce CO_2 and OH – bearing phases during cooling (possibly at 400–600°C; Carvalho *et al.*, 2020). Pure CO_2 inclusions within garnets are also present, which might represent the fluid that infiltrated into the rocks at a very late stage.

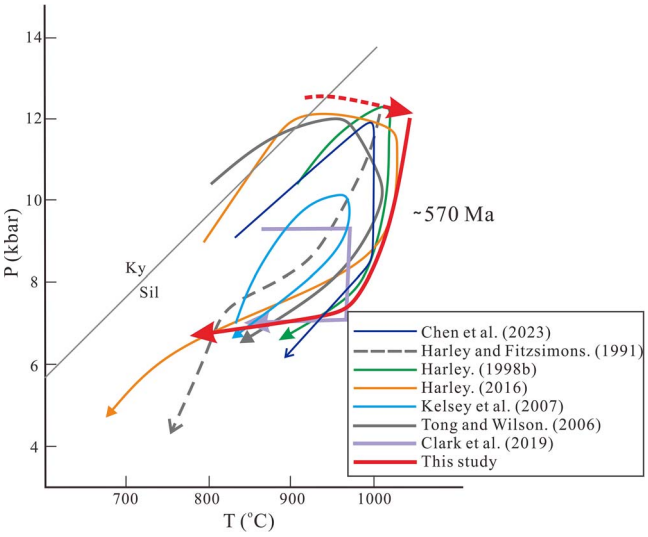

Fig. 15. Suggested *P–T* path of *UHT* granulites from the Mather Peninsula, East Antarctica. Also shown are previously retrieved *P–T* paths for the *UHT* granulites from the Rauer Islands (modified after Tong *et al.*, 2021).

In regard of the origin of the fluid, several potential sources can be considered. Harley *et al.* (1998) speculated that the infiltration of CO_2-rich fluid might have occurred during the decompression as a consequence of emplacements of granitic pegmatites in the Cambrian (Kinny *et al.*, 1993). Additionally, coeval graphite-bearing sediments (e.g. Harley & Fitzsimons, 1991) and forsterite marbles (e.g. Buick et al., 1994; Harley, 1998b) have been reported in the Rauer Islands, and their decarbonation may also be external sources for the fluid. Collectively, an external source for the C–O–H fluid is favored in this study. Fluid infiltration not only lead to possible transfer of fluid-related elements (e.g. Liu *et al.*, 2018), but also caused partial to complete resetting of U–Th–Pb systems in zircon and monazite (e.g. Harley *et al.*, 1998; Harley & Kelly, 2007; Taylor *et al.*, 2014; Das *et al.*, 2021).

As addressed on the section of geological setting, the timing of the *UHT* metamorphism is still a matter of debate. Constraints on its timing are critical to understanding the tectonothermal evolution of the Rauer Islands, and even the whole Prydz Belt. Some works proposed that the Prydz Belt represents an early Neoproterozoic (~1000 Ma) metamorphic complex that was reworked by a Pan–African (~530 Ma) thermal event (e.g. Wang *et al.*, 2008; Liu *et al.*, 2009, 2014; Tong *et al.*, 2014b, 2019), and the *UHT* metamorphism in the Rauer Islands occurred at ~1000 Ma (Tong & Wilson, 2006; Wang *et al.*, 2007). This point of view has not been accepted by other researchers, who argued that this episode of *UHT* metamorphism may have taken place in the late Neoproterozoic to Cambrian (e.g. Kelsey *et al.*, 2003, 2007; Clark *et al.*, 2019) or prior to ~590 Ma (Harley *et al.*, 2009; Hokada *et al.*, 2016). Our dating results for zircon mantles show variable dates ranging from 1050 to 607 Ma (Fig. 12e; Table 5). Previous U–Pb dating on Spr – bearing *UHT* granulites from the same locality also showed similar age spreads from 1000 Ma to 500 Ma (Wang *et al.*, 2007; Hokada *et al.*, 2016). Such scattered ages were previously interpreted as mixed ages, detrital ages, or ascribed to variable effects of the Pan–African thermal event on pre-existing zircons (Hokada *et al.*, 2016; Spreitzer *et al.*, 2021; Wang *et al.*, 2022). Although we cannot preclude the possibility of melt-mediated-coupled dissolution-precipitation of zircons in the Cambrian (Wang *et al.*, 2022), findings of secondary FIs in

peritectic phases (such as garnet, orthopyroxene) and zircons in this study seem to support that the broad range of isotopic dates may be partially caused by extensive C–O–H fluid infiltration at high temperature conditions (>600°C). Till now, all the U–Th–Pb dating on monazite pointed to metamorphic ages of 580–510 Ma (Clark et al., 2018; Hokada *et al.*, 2016; Kelsey *et al.*, 2003, 2007; Liu *et al.*, 2021). Here, we prefer the interpretation that U–Th–Pb clock of monazites has been completely reset as they were more vulnerable to fluid ingress compared with zircons (e.g. Taylor *et al.*, 2014; Das *et al.*, 2021).

Additionally, garnet inclusions within zircon mantles from mafic granulites in the Archean crustal domain indicate that the post-peak decompression and cooling probably occurred at 540–471 Ma (our own unpublished data), roughly consistent with the dates documented by zircon rims in this study (569–472 Ma). If it is the case, the peak metamorphism took place at least prior to ~570 Ma. Hokada *et al.* (2016) reported the microstructure and CL image of an orthopyroxene–hosted zircon inclusion from the same outcrop, and it documents ages of 2502 Ma in the core and 1254–1148 Ma in the rim. This suggests that this type of zircons has not been affected by the Pan–African thermal event likely due to the shielding effect of orthopyroxene. Five dark-CL mantles show $^{206}Pb/^{238}U$ dates of 1050–940 Ma (Table 5), which however, are slightly discordant (Fig. 12f). Up to now, the most concordant ages for the Spr-bearing *UHT* granulites from the Mather Peninsula were obtained by Wang *et al.* (2007), which yielded a weighted mean $^{207}Pb/^{206}Pb$ age of 995 ± 15 Ma. Nonetheless, their dating results also showed some discordance from 1000 Ma toward 530 Ma (Wang *et al.*, 2007). The present study highlights that C–O–H fluid infiltration and alternatively, melt-mediated-coupled dissolution-precipitation during the Pan–African reworking, have contributed to the partial resetting of U–Th–Pb systems in zircons. Collectively, the *P–T* framework (Fig. 15) might be linked with two separated thermal events that happened at ~1000 Ma and ~530 Ma, respectively. We propose that the *UHT* metamorphism and relevant melting most likely occurred prior to ~570 Ma (Harley *et al.*, 2009; Hokada *et al.*, 2016), while the post-peak decompression and the final cooling happened at 570–470 Ma (Fig. 15). However, it is still far from precisely determining the timing of *UHT* metamorphism in this region, which requires further investigations.

CONCLUSIONS

Phase equilibria modeling suggests that the Spr-bearing *UHT* granulites from the Mather Peninsula (East Antarctica) have undergone a clockwise *P–T* path, with peak conditions of 12–13 kbar and 1070–1130°C. Melt and fluid inclusions are characterized in this study. Coupled with chronological dating results, the main conclusions drawn are described below:

(1) Abundant NIs are preserved within garnet, which are usually 5–15 μm in diameter and display typically negative crystal shapes. NIs have crystallized into polycrystalline aggregates, comprising daughter phases of quartz, biotite, kokchetavite, kumdykolite and an unknown phase (phase '430'). Petrographic observations and mineral chemistry suggest that the melts were at least partially yielded at *UHT* conditions. The NIs were perfectly re – homogenized with a piston cylinder apparatus at ~12 kbar and ~950°C, and show SiO_2-rich, strongly peraluminous and potassic to ultrapotassic composition.

(2) Compared with the granulitic restite, the NIs are enriched in Li, Cs, Rb, Ta, Sm, Nd, Zr, U and Pb, and depleted in Ce, Th, Ba, Sr and Nb. Melting mechanisms and dissolution of accessory minerals played a key role in the partitioning of elements between anatectic melts and their granulitic counterparts. High Rb/Sr and Sm/Nd ratios for the melts, coupled with phase equilibria modeling, suggest that the melts were formed by fluid–absent Bt – dehydration melting. These *UHT* crustal melts have densities of 2.47 ± 0.07 g/cm^3, viscosities of $10^{4.9\pm1.2}$ Pa·s and high heat production values of ~2.8 μW/m^3. As a consequence, these melts are expected to be mobile and may have played an important role in redistribution of heat–producing elements (such as K and U).

3) Secondary FIs are distributed along healed fractures of the peritectic phases (such as garnet and orthopyroxene), typically comprising magnesite, corundum, pyrophyllite and residual CO_2 (ρ_{CO2} = 0.2–1.0 g/cm^3). They are interpreted as stepdaughter phases due to interaction between C – O – H fluid and their hosts during post–peak metamorphic evolutions. Pure CO_2 inclusions with a density of ~0.8 are also present, representing the fluid that infiltrated the rock at a very late stage. Ingress of the C–O–H fluid under high temperatures probably resulted in mobility and loss of Pb in zircons, and was likely responsible for the large date span of zircon mantles from 1050 to 607 Ma. Another possible reason is melt-mediated-coupled dissolution-precipitation during the Pan–African reworking. Therefore, the retrieved *P–T* path might be linked with two separated thermal events happened at ~1000 and ~530 Ma, respectively. Although metamorphic timing for the UHT metamorphism is still debated, we conclude that the peak metamorphism occurred prior to ~570 Ma.

DATA AVAILABILITY

The authors confirm that the data cited in Fig. 11 of this manuscript are available within the the paper of Acosta Vigil *et al.* (2010).

Supplementary Data

Supplementary data are available at *Journal of Petrology* online.

ACKNOWLEDGEMENTS

This research was financially supported by the NSFC projects (42102043, 41972050) and the China Postdoctoral Science Foundation (2020 M683535). This study also benefitted from funding of the Programma Nazionale di Ricerca in Antartide 2018 (PNRA18_00103 to B.B. Carvalho) and Padua University (BART_SID19_01 to O. Bartoli; WelcomeKit to B.B. Carvalho). We thank the leaders and members of the 33rd and 39th Chinese National Antarctic Research Expedition (CHINARE) for the logistic support during the Antarctic field work. We are especially grateful to Prof. J. Liu for his involvement in the field work. Dr. W.Q. Yang and Dr. C. Li are thanked for his help in the electronic microprobe analyses for mineral compositions. Dr. Y.G. Feng from Chang'an University is acknowledged for his help in the Raman analyses. We are deeply indebted to Dr. J.Y. Pan, J.M. Cui and J.Y. Ding from Nanjing University for their kind help during the LA – ICP – MS analyses for trace element of melt inclusions. We are grateful to Prof. Georg Zellmer (editor–in–chief) and Sherlock Sarah (editor) for their editorial work, and Alessia Borghini, Tetsuo Kawakami and Jon Pownall for their constructive comments that greatly improved the paper.

References

Acosta Vigil, A., Buick, I., Hermann, J., Cesare, B., Rubatto, D., London, D. & Morgan VI, G. B. (2010). Mechanisms of crustal anatexis: a geochemical study of partially melted metapelitic enclaves and

host dacite, SE Spain. *Journal of Petrology* **51**, 785–821. https://doi.org/10.1093/petrology/egp095.

Acosta Vigil, A., London, D. & Morgan, G. B. (2012). Chemical diffusion of major components in granitic liquids: implications for the rates of homogenization of crustal melts. *Lithos* **153**, 308–323. https://doi.org/10.1016/j.lithos.2012.06.017.

Artemieva, I. M., Thybo, H., Jakobsen, K., Sørensen, N. K. & Nielsen, L. S. K. (2017). Heat production in granitic rocks: global analysis based on a new data compilation GRANITE2017. *Earth-Science Reviews* **172**, 1–26. https://doi.org/10.1016/j.earscirev.2017.07.003.

Bartoli, O. (2017). Phase equilibria modelling of residual migmatites and granulites: an evaluation of the melt-reintegration approach. *Journal of Metamorphic Geology* **35**, 919–942. https://doi.org/10.1111/jmg.12261.

Bartoli, O. (2019). Reintegrating nanogranitoid inclusion composition to reconstruct the prograde history of melt-depleted rocks. *Geoscience Frontiers* **10**, 517–525. https://doi.org/10.1016/j.gsf.2018.02.002.

Bartoli, O. & Carvalho, B. B. (2021). Anatectic granites in their source region: a comparison between experiments, thermodynamic modelling and nanogranitoids. *Lithos* **402–403**, 106046. https://doi.org/10.1016/j.lithos.2021.106046.

Bartoli, O., Cesare, B., Poli, S., Acosta Vigil, A., Esposito, R., Turina, A., Bodnar, R. J., Angel, R. J. & Hunter, J. (2013a). Nanogranite inclusions in migmatitic garnet: behavior during piston-cylinder remelting experiments. *Geofluids* **13**, 405–420. https://doi.org/10.1111/gfl.12038.

Bartoli, O., Cesare, B., Poli, S., Bodnar, R. J., Acosta Vigil, A., Frezzotti, M. L. & Meli, S. (2013b). Recovering the composition of melt and the fluid regime at the onset of crustal anatexis and S-type granite formation. *Geology* **41**, 115–118. https://doi.org/10.1130/G33455.1.

Bartoli, O., Cesare, B., Remusat, L., Acosta Vigil, A. & Poli, S. (2014). The H_2O content of granite embryos. *Earth and Planetary Science Letters* **395**, 281–290. https://doi.org/10.1016/j.epsl.2014.03.031.

Bartoli, O., Acosta Vigil, A., Ferrero, S. & Cesare, B. (2016). Granitoid magmas preserved as melt inclusions in high-grade metamorphic rock. *American Mineralogist* **101**, 1543–1559. https://doi.org/10.2138/am-2016-5541CCBYNCND.

Bartoli, O., Acosta-Vigil, A., Cesare, B., Remusat, L., Gonzalez-Cano, A., Wälle, M., Tajčmanová, L. & Langone, A. (2019). Geochemistry of Eocene-Early Oligocene low-temperature crustal melts from Greater Himalayan sequence (Nepal): a nanogranitoid perspective. *Contributions to Mineralogy and Petrology* **174**, 82. https://doi.org/10.1007/s00410-019-1622-2.

Bea, F. (2012). The sources of energy for crustal melting and the geochemistry of heat producing elements. *Lithos* **153**, 278–291. https://doi.org/10.1016/j.lithos.2012.01.017.

Berkesi, M., Hidas, K., Guzmics, T., Dubessy, J., Bodnar, R. J., Szabó, C., Vajna, B. & Tsunogae, T. (2009). Detection of small amounts of H_2O in CO_2-rich fluid inclusions using Raman spectroscopy. *Journal of Raman Spectroscopy* **40**, 1461–1463. https://doi.org/10.1002/jrs.2440.

Borghini, A., Ferrero, S., Wunder, B., Laurent, O., O'Brien, P. J. & Ziemann, M. A. (2018). Granitoid melt inclusions in orogenic peridotite and the origin of garnet clinopyroxenite. *Geology* **46**, 1007–1010. https://doi.org/10.1130/G45316.1.

Borghini, A., Nicoli, G., Ferrero, S., O'Brien, P. J., Laurent, O., Remusat, L., Borghini, G. & Milani, S. (2023). The role of continental subduction in mantle metasomatism and carbon recycling revealed by melt inclusions in UHP eclogites. *Science Advances* **9**, eabp9482. https://doi.org/10.1126/sciadv.abp9482.

Brown, M. (2007). Metamorphic conditions in orogenic belts: a record of secular change. *International Geology Review* **49**, 193–234. https://doi.org/10.2747/0020-6814.49.3.193.

Brown, M. (2013). Granite: from genesis to emplacement. *GSA Bulletin* **125**, 1079–1113. https://doi.org/10.1130/B30877.1.

Carvalho, B. B., Bartoli, O., Ferri, F., Cesare, B., Ferrero, F., Remusat, L., Capizzi, L. & Poli, S. (2019). Anatexis and fluid regime of the deep continental crust: new clues from melt and fluid inclusions in metapelitic migmatites from Ivrea zone (NW Italy). *Journal of Metamorphic Geology* **37**, 951–975. https://doi.org/10.1111/jmg.12463.

Carvalho, B. B., Bartoli, O., Cesare, B., Tacchetto, T., Gianola, O., Ferri, F., Aradi, L. E. & Szabó, C. (2020). Primary CO_2-bearing fluid inclusions in granulitic garnet usually do not survive. *Earth and Planetary Science Letters* **536**, 116170. https://doi.org/10.1016/j.epsl.2020.116170.

Carvalho, B. B., Bartoli, O., Cesare, B., Satish Kumar, M., Petrelli, M., Kawakami, T., Hokada, T. & Gilio, M. (2023a). Revealing the link between A-type granites and hottest melts from residual metasedimentary crust. *Geology*. Doi.org/10.1130/G51097.1.

Carvalho, B. B., Bartoli, O. & Cesare, C. (2023b). C–O–H fluid–melt–rock interaction in graphitic granulites and problems of quantifying carbon budget in the lower continental crust. *Chemical Geology* **631**, 121503. https://doi.org/10.1016/j.chemgeo.2023.121503.

Cavalcante, G. C. G., Viegas, G., Archanjo, C. J. & da Silva, M. E. (2016). The influence of partial melting and melt migration on the rheology of the continental crust. *Journal of Geodynamics* **101**, 186–199. https://doi.org/10.1016/j.jog.2016.06.002.

Cenki, B., Kriegsman, L. M. & Braun, I. (2002). Melt—producing and melt—consuming reactions in anatectic granulites: P–T evolution of the Achankovil cordierite gneisses, South India. *Journal of Metamorphic Geology* **20**, 543–561. https://doi.org/10.1046/j.1525-1314.2002.00388.x.

Cesare, B., Satish Kumar, M., Cruciani, G., Pocker, S. & Nodari, L. (2008). Mineral chemistry of Ti-rich biotite from pegmatite and metapelitic granulites of the Kerala Khondalite Belt (Southeast India): petrology and further insight into titanium substitutions. *American Mineralogist* **93**, 327–338. https://doi.org/10.2138/am.2008.2579.

Cesare, B., Ferrero, S., Salvioli Mariani, E., Pedron, D. & Cavallo, A. (2009). Nanogranite and glassy inclusions: the anatectic melt in migmatites and granulites. *Geology* **37**, 627–630. https://doi.org/10.1130/G25759A.1.

Cesare, B., Acosta Vigil, A., Bartoli, O. & Ferrero, S. (2015). What can we learn from melt inclusions in migmatites and granulites? *Lithos* **239**, 186–216. https://doi.org/10.1016/j.lithos.2015.09.028.

Chappell, B. W. (1999). Aluminium saturation in I– and S—type granites and the characterization of fractionated haplogranites. *Lithos* **46**, 535–551. https://doi.org/10.1016/S0024-4937(98)00086-3.

Chen, L. Y., Liu, X. C., Wang, W.-R. Z. & Liu, J. (2023). Ultrahigh-temperature mafic Granulites in the Rauer group, East Antarctica: evidence from conventional Thermobarometry, phase equilibria modeling, and rare earth element thermometry. *Journal of Petrology* **64**, 1–28. https://doi.org/10.1093/petrology/egad014.

Clark, C., Fitzsimons, I. C. W., Healy, D. & Harley, S. L. (2011). How does the continental crust get really hot? *Elements* **7**, 235–240. https://doi.org/10.2113/gselements.7.4.235.

Clark, C., Taylor, R. J. M., Johnson, T. E., Harley, S. L., Fitzsimons, I. C. W. & Oliver, L. (2019). Testing the fidelity of thermometers at ultrahigh temperatures. *Journal of Metamorphic Geology* **37**, 917–934. https://doi.org/10.1111/jmg.12486.

Clemens, J. D. & Vielzeuf, D. (1987). Constraints on melting and magma production in the crust. *Earth and Planetary Science Letters* **86**, 287–306. https://doi.org/10.1016/0012-821X(87)90227-5.

Clemens, J. D., Stevens, G. & Bryan, S. E. (2020). Conditions during the formation of granitic magmas by crustal melting hot or cold; drenched, damp or dry? *Earth-Science Reviews* **200**, 102982. https://doi.org/10.1016/j.earscirev.2019.102982.

Connolly, J. A. D. (2005). Computation of phase equilibria by linear programming: a tool for geodynamic modeling and its application to subduction zone decarbonation. *Earth and Planetary Science Letters* **236**, 524–541. https://doi.org/10.1016/j.epsl.2005.04.033.

Das, K., Bose, S., Torimoto, J., Hayasaka, Y. & Dunkley, D. (2021). Tracking C–O–H fluid–rock interactions in reworked UHT granulite: tectonic evolution from ca. 990 ma to ca. 500 ma in orogenic interior of eastern Ghats Belt, India. *Lithos* **398–399**, 106287.

Diener, J. F. A. & Fagereng, Å. (2014). The influence of melting and melt drainage on crustal rheology during orogenesis. *Journal of Geophysical Research: Solid Earth* **119**, 6193–6210. https://doi.org/10.1002/2014JB011088.

Dirks, P. H. G. M. & Wilson, C. J. L. (1995). Crustal evolution of the East Antarctic mobile belt in Prydz Bay: continental collision at 500Ma? *Precambrian Research* **75**, 189–207. https://doi.org/10.1016/0301-9268(95)80006-4.

Droop, G. T. R., Clemens, J. D. & Dalrymple, D. J. (2003). Processes and conditions during contact anatexis, melt escape and restite formation: the Huntly gabbro complex, NE Scotland. *Journal of Petrology* **44**, 995–1029. https://doi.org/10.1093/petrology/44.6.995.

Ewing, T. A., Hermann, J. & Rubatto, D. (2013). The robustness of the Zr–in–rutile and Ti–in–zircon thermometers during high-temperature metamorphism (Ivrea-Verbano zone, northern Italy). *Contributions to Mineralogy and Petrology* **165**, 757–779. https://doi.org/10.1007/s00410-012-0834-5.

Ferrero, S. & Angel, R. J. (2018). Micropetrology: are inclusions grains of truth? *Journal of Petrology* **59**, 1671–1700. https://doi.org/10.1093/petrology/egy075.

Ferrero, S., Bartoli, O., Cesare, B., Salvioli Mariani, E., Acosta Vigil, A., Cavallo, A., Groppo, C. & Battiston, S. (2012). Microstructures of melt inclusions in anatectic metasedimentary rocks. *Journal of Metamorphic Geology* **30**, 303–322. https://doi.org/10.1111/j.1525-1314.2011.00968.x.

Ferrero, S., Ziemann, M. A., Angel, R. J., O'Brien, P. J. & Wunder, B. (2016). Kumdykolite, kokchetavite, and cristobalite crystallized in nanogranites from felsic granulites, Orlica-Snieznik dome (Bohemian Massif): not an evidence for ultrahigh-pressure conditions. *Contributions to Mineralogy and Petrology* **171**, 3. https://doi.org/10.1007/s00410-015-1220-x.

Ferrero, S., Godard, G., Palmeri, R., Wunder, B. & Cesare, B. (2018). Partial melting of ultramafic granulites from Dronning Maud land, Antarctica: constraints from melt inclusions and thermodynamic modelling. *American Mineralogist* **103**, 610–622. https://doi.org/10.2138/am-2018-6214.

Ferrero, S., Wannhoff, I., Laurent, O., Yakymchuk, C., Darling, C., Wunder, B., Borghini, A. & O'Brien, P. J. (2021a). Embryos of TTGs in Gore Mountain garnet megacrysts from water–fluxed melting of the lower crust. *Earth and Planetary Science Letters* **569**, 117058. https://doi.org/10.1016/j.epsl.2021.117058.

Ferrero, S., Ague, J. J., O'Brien, P. J., Wunder, B., Remusat, L., Ziemann, A. & Axler, J. (2021b). High pressure, halogen–bearing melt preserved in ultra–high temperature felsic granulites of the Central Maine Terrane, Connecticut (US). *American Mineralogist* **106**, 1225–1236. https://doi.org/10.2138/am-2021-7690.

Ferri, F., Cesare, B., Bartoli, O., Ferrero, S., Palmeri, R., Remusat, L. & Poli, S. (2020). Melt inclusions at MT. Edixon (Antarctica): chemistry, petrology and implications for the evolution of the Lanterman range. *Lithos* **374–375**, 105685.

Fitzsimons, I. C. W. (2003). Proterozoic basement provinces of southern and southwestern Australia, and their correlation with Antarctica. *Geological Society, London, Special Publications* **206**, 93–130. https://doi.org/10.1144/GSL.SP.2003.206.01.07.

Frezzotti, M. L., Tecce, F. & Casagli, A. (2012). A. Raman spectroscopy for fluid inclusion analysis. *Journal of Geochemical Exploration* **112**, 1–20. https://doi.org/10.1016/j.gexplo.2011.09.009.

Frost, B. R. & Frost, C. D. (2008). A geochemical classification for feldspathic igneous rocks. *Journal of Petrology* **49**, 1955–1969. https://doi.org/10.1093/petrology/egn054.

Galli, A., Le Bayon, B., Schmidt, M. W., Burg, J. P., Reusser, E., Sergeev, S. A. & Larionov, A. (2012). U–Pb zircon dating of the Gruf complex: disclosing the late Variscan granulitic lower crust of Europe stranded in the Central Alps. *Contributions to Mineralogy and Petrology* **163**, 353–378. https://doi.org/10.1007/s00410-011-0676-6.

Gao, Y. J. & Liu, J. B. (2018). Research advances of melt inclusions in high-grade metamorphic rocks. *Earth Science* **43**, 236–246 (in Chinese with English abstract).

Gao, X. Y., Zheng, Y. F., Chen, Y. X. & Hu, Z. (2014). Composite carbonate and silicate multiphase solid inclusions in metamorphic garnet from ultrahigh–P eclogite in the Dabie orogen. *Journal of Metamorphic Geology* **32**, 961–980. https://doi.org/10.1111/jmg.12102.

Gao, P., Zheng, Y. F. & Zhao, Z. F. (2016). Experimental melts from crustal rocks: a lithochemical constraint on granite petrogenesis. *Lithos* **266-267**, 133–157. https://doi.org/10.1016/j.lithos.2016.10.005.

Gao, L. E., Zeng, L. & Asimow, P. D. (2017). Contrasting geochemical signatures of fluid–absent versus fluid-fluxed melting of muscovite in metasedimentary sources: the Himalayan leucogranites. *Geology* **45**, 39–42. https://doi.org/10.1130/G38336.1.

Gianola, O., Bartoli, O., Ferri, F., Galli, A., Ferrero, S., Capizzi, L. S., Liebske, C., Remusat, L., Poli, S. & Cesare, B. (2021). Anatectic melt inclusions in ultra high temperature granulites. *Journal of Metamorphic Geology* **39**, 321–342. https://doi.org/10.1111/jmg.12567.

Giordano, D., Russell, J. K. & Dingwell, D. B. (2008). Viscosity of magmatic liquids: a model. *Earth and Planetary Science Letters* **271**, 123–134. https://doi.org/10.1016/j.epsl.2008.03.038.

Grew, E. S., Carson, C. J., Christy, A. G., Maas, R., Yaxley, G. M., Boger, S. D. & Fanning, C. M. (2012). New constraints from U–Pb, Lu–Hf and Sm–Nd isotopic data on the timing of sedimentation and felsic magmatism in the Larsemann Hills, Prydz Bay, East Antarctica. *Precambrian Research* **206-207**, 87–108. https://doi.org/10.1016/j.precamres.2012.02.016.

Guillong, M., Meier, D. L., Allan, M. M., Heinrich, C. A. & Yardley, B. W. D. (2008). SILLS: a MATLAB-based program for the reduction of laser ablation ICP–MS data of homogeneous materials and inclusions. *Mineralogical Association of Canada Short Course* **40** Vancouver, 328–333.

Halter, W. E., Pettke, T., Heinrich, C. A. & Rothen Rutishauser, B. (2002). Major to trace element analysis of melt inclusions by laser-ablation ICP–MS: methods of quantification. *Chemical Geology* **183**, 63–86. https://doi.org/10.1016/S0009-2541(01)00372-2.

Harley, S. L. (1998a). On the occurrence and characterization of ultrahigh temperature crustal metamorphism. *Geological Society, London, Special Publications* **138**, 81–107. https://doi.org/10.1144/GSL.SP.1996.138.01.06.

Harley, S. L. (1998b). Ultrahigh temperature granulite metamorphism (1050 °C, 12 kbar) and decompression in garnet (Mg70)–orthopyroxene–sillimanite gneisses from the Rauer group, East

Antarctica. *Journal of Metamorphic Geology* **16**, 541–562. https://doi.org/10.1111/j.1525-1314.1998.00155.x.

Harley, S. L. (2008). Refining the P–T records of UHT crustal metamorphism. *Journal of Metamorphic Geology* **26**, 125–154. https://doi.org/10.1111/j.1525-1314.2008.00765.x.

Harley, S. L. (2016). A matter of time: the importance of the duration of UHT metamorphism. *Journal of Mineralogical and Petrological Sciences* **111**, 50–72. https://doi.org/10.2465/jmps.160128.

Harley, S. L. (2021) UHT metamorphism. In: Alderton D. & Elias S. A. (eds) *Encyclopedia of Geology*, 2nd edn. United Kindom: Academic Press. Vol 2, pp.522–552.

Harley, S. L. & Fitzsimons, I. C. W. (1991). Pressure–temperature evolution of metapelitic granulites in a polymetamorphic terrane: the Rauer group, East Antarctica. *Journal of Metamorphic Geology* **9**, 231–243. https://doi.org/10.1111/j.1525-1314.1991.tb00519.x.

Harley, S. L. & Kelly, N. M. (2007). The impact of zircon–garnet REE distribution data on the interpretation of zircon U–Pb ages in complex high-grade terrains: an example from the Rauer Islands, East Antarctica. *Chemical Geology* **241**, 62–87. https://doi.org/10.1016/j.chemgeo.2007.02.011.

Harley, S. L., Snape, I. & Fitzsimons, I. C. W. (1995). Regional correlations and terrane assembly in east Prydz Bay: evidence from the Rauer group and Vestfold Hills. *Terra Antarcica* **2**, 49–60.

Harley, S. L., Snape, I. & Black, L. P. (1998). The early evolution of a layered metaigneous complex in the Rauer group, East Antarctica: evidence for a distinct Archaean terrane. *Precambrian Research* **89**, 175–205. https://doi.org/10.1016/S0301-9268(98)00031-X.

Harley, S. L., Hokada, T., Montel, J. M. & Parseval, P. (2009, 2009) Sapphirine + quartz in the Rauer Islands, Antarctica: evidence for 590 Ma UHT metamorphism and melting. In: *Abstract of Granulites & Granulites Conference*.

Harley, S. L., Fitzsimons, I. C. W. & Zhao, Y. (2013) Antarctica and supercontinent evolution: historical perspectives, recent advances and unresolved issues. In: Harley S. L., Fitzsimons I. C. W. & Zhao Y. (eds) *Antarctica and Supercontinent Evolution*. London: Geological Society of London Special Publications, 383, pp.1–34.

Hensen, B. J. & Zhou, B. (1997) East Gondwana amalgamation by Pan–African collision? Evidence from Prydz Bay, East Antarctica. In: Ricci C. A. (ed) *The Antarctic Region; Geological Evolution and Processes*. Terra Antartica, Siena 7: International Symposium on Antarctic Earth Sciences, pp.115–119.

Hess, K. U. & Dingwell, D. B. (1996). Viscosities of hydrous leucogranitic melts: a non-Arrhenian model. *American Mineralogist* **81**, 1297–1300.

Higashino, F. & Kawakami, T. (2022). Ultrahigh-temperature metamorphism and melt inclusions from the Sør Rondane Mountains, East Antarctica. *Journal of Mineralogical and Petrological Sciences* **117**, n/a. https://doi.org/10.2465/jmps.220325.

Hiroi, Y., Hokada, T., Kato, M., Yanagi, A., Adachi, T., Osanai, Y., Mototoshi, Y. & Shiraishi, K. (2019). Felsite–nanogranite inclusions and three Al_2SiO_5 polymorphs in the same garnet in ultrahigh-temperature granulites from Rundvågshetta, Lützow–Holm complex, East Antarctica. *Journal of Mineralogical and Petrological Sciences* **114**, 60–78. https://doi.org/10.2465/jmps.181118.

Hokada, T., Harley, S. L., Dunkley, D. J., Kelly, N. M. & Yokayama, K. (2016). Peak and post-peak development of UHT metamorphism at Mather peninsula, Rauer Islands: zircon and monazite U–Th–Pb and REE chemistry constraints. *Journal of Mineralogical and Petrological Sciences* **111**, 89–103. https://doi.org/10.2465/jmps.150829.

Holland, T. J. B. & Powell, R. (2011). An improved and extended internally consistent thermodynamic dataset for phases of petrological interest, involving a new equation of state for solids. *Journal of Metamorphic Geology* **29**, 333–383. https://doi.org/10.1111/j.1525-1314.2010.00923.x.

Holness, M. B., Cesare, B. & Sawyer, E. W. (2011). Melted rocks under the microscope: microstructures and their interpretation. *Elements* **7**, 247–252. https://doi.org/10.2113/gselements.7.4.247.

Holtz, F., Johannes, W., Tamic, N. & Behrens, H. (2001). Maximum and minimum water contents of granitic melts generated in the crust: a reevaluation and implications. *Lithos* **56**, 1–14. https://doi.org/10.1016/S0024-4937(00)00056-6.

Hu, Z. C., Zhang, W., Liu, Y. S., Gao, S., Li, M., Zong, K. Q., Chen, H. H. & Hu, S. H. (2015). "Wave" signal-smoothing and mercury-removing device for laser ablation quadrupole and multiple collector ICPMS analysis: application to lead isotope analysis. *Analytical Chemistry* **87**, 1152–1157. https://doi.org/10.1021/ac503749k.

Huang, G., Guo, J., Jiao, S. J. & Palin, R. (2019). What drives the continental crust to be extremely hot so quickly? *Journal of Geophysical Research: Solid Earth* **124**, 11218–11231. https://doi.org/10.1029/2019JB017840.

Huang, G., Guo, J. & Palin, R. (2021). Phase equilibria modeling of anatexis during ultra-high temperature metamorphism of the crust. *Lithos* **398–399**, 106326. https://doi.org/10.1016/j.lithos.2021.106326.

Hwang, S. L., Shen, P., Chu, H. T., Yui, T. F., Liou, J. G., Sobolev, N. V., Zhang, R. Y., Shatsky, V. S. & Zayachkovsky, A. A. (2004). Kokchetavite: a new polymorph of $KAlSi_3O_8$ from the Kokchetav UHP terrain. *Contributions to Mineralogy and Petrology* **148**, 380–389. https://doi.org/10.1007/s00410-004-0610-2.

Hwang, S. L., Shen, P., Chu, H. T., Yui, T. F., Liou, J. G. & Sobolev, N. V. (2009). Kumdykolite, an orthorhombic polymorph of albite, from the Kokchetav ultrahigh-pressure massif, Kazakhstan. *European Journal of Mineralogy* **21**, 1325–1334. https://doi.org/10.1127/0935-1221/2009/0021-1970.

Hwang, S. L., Yui, T. F., Chu, H. T., Shen, P., Liou, J. G. & Sobolev, N. V. (2013). Oriented kokchetavite compound rods in clinopyroxene of Kokchetav ultrahigh-pressure rocks. *Journal of Asian Earth Sciences* **63**, 56–69. https://doi.org/10.1016/j.jseaes.2012.09.003.

Iacovino, K. & Till, C. B. (2019). DensityX: a program for calculating the densities of magmatic liquids up to 1,627 °C and 30 kbar. *Volcanica* **2**, 1–10. https://doi.org/10.30909/vol.02.01.0110.

Jackson, S. E., Pearson, N. J., Griffin, W. L. & Belousova, E. A. (2004). The application of laser ablation–inductively coupled plasma–mass spectrometry to in situ U–Pb zircon geochronology. *Chemical Geology* **211**, 47–69. https://doi.org/10.1016/j.chemgeo.2004.06.017.

Kawakami, T. & Motoyoshi, Y. (2004). Timing of attainment of the spinel + quartz coexistence in garnet–sillimanite leucogneiss from Skallevikshalsen, Lützow–holm complex, East Antarctica. *Journal of Mineralogical and Petrological Sciences* **99**, 311–319. https://doi.org/10.2465/jmps.99.311.

Kelsey, D. E. & Powell, R. (2011). Progress in linking accessory mineral growth and breakdown to major mineral evolution in metamorphic rocks: a thermodynamic approach in the Na_2O–CaO–K_2O–FeO–MgO–Al_2O_3–SiO_2–H_2O–TiO_2–ZrO_2 system. *Journal of Metamorphic Geology* **29**, 151–166. https://doi.org/10.1111/j.1525-1314.2010.00910.x.

Kelsey, D. E., Powell, R., Wilson, C. J. L. & Steele, D. A. (2003). (Th+U)–Pb monazite ages from Al–Mg-rich metapelites, Rauer group East Antarctica. *Contributions to Mineralogy and Petrology* **146**, 326–340. https://doi.org/10.1007/s00410-003-0497-3.

Kelsey, D. E., Hand, M., Clark, C. & Wilson, C. J. L. (2007). On the application of in situ monazite chemical geochronology to constraining P–T–t histories in high-temperature (>850 ° C) polymetamorphic granulites from Prydz Bay, East Antarctica.

Journal of the Geological Society, London **164**, 667–683. https://doi.org/10.1144/0016-76492006-013.

Kinny, P. D., Black, L. P. & Sheraton, J. W. (1993). Zircon ages and distribution of Archaean and Proterozoic rocks in the Rauer Island. *Antarctic Science* **5**, 193–206. https://doi.org/10.1017/S0954102093000252.

Korhonen, F. J., Powell, R. & Stout, J. H. (2012). Stability of sapphirine plus quartz in the oxidized rocks of the Wilson Lake terrane, Labrador: calculated equilibria in NCKFMASHTO. *Journal of Metamorphic Geology* **30**, 21–36. https://doi.org/10.1111/j.1525-1314.2011.00954.x.

Kotková, J., Škoda, R. & Machovič, V. (2014). Kumdykolite from the ultrahigh-pressure granulite of the Bohemian Massif. *American Mineralogist* **99**, 1798–1801. https://doi.org/10.2138/am.2014.4889.

Lamadrid, H. M., Lamb, W. M., Santosh, M. & Bodnar, R. J. (2014). Raman spectroscopic characterization of H_2O in CO_2-rich fluid inclusions in granulite facies metamorphic rocks. *Gondwana Research* **26**, 301–310. https://doi.org/10.1016/j.gr.2013.07.003.

Lei, H. & Xu, H. (2018). A review of ultrahigh temperature metamorphism. *Journal of Earth Science* **29**, 1167–1180. https://doi.org/10.1007/s12583-018-0846-9.

Li, X. C., Zhou, M. F., Chen, W. T., Zhao, X. F. & Tran, M. (2018). Uranium–lead dating of hydrothermal zircon and monazite from the sin Quyen Fe–Cu–REE–Au–(U) deposit, northwestern Vietnam. *Mineralium Deposita* **53**, 399–416. https://doi.org/10.1007/s00126-017-0746-4.

Liu, Y. S., Hu, Z. C., Gao, S., Günther, D., Xu, J., Gao, C. G. & Chen, H. H. (2008). In situ analysis of major and trace elements of anhydrous minerals by LA–ICP–MS without applying an internal standard. *Chemical Geology* **257**, 34–43. https://doi.org/10.1016/j.chemgeo.2008.08.004.

Liu, X., Zhao, Y., Song, B., Liu, J. & Cui, J. (2009). SHRIMP U–Pb zircon geochronology of high–grade rocks and charnockites from the eastern Amery ice shelf and southwestern Prydz Bay, East Antarctica: constraints on late Mesoproterozoic to Cambrian tectonothermal events related to supercontinent assembly. *Gondwana Research* **16**, 342–361. https://doi.org/10.1016/j.gr.2009.02.003.

Liu, Y. S., Gao, S., Hu, Z. C., Gao, C. G., Zong, K. Q. & Wang, D. B. (2010). Continental and oceanic crust recycling-induced melt–peridotite interactions in the Trans–North China Orogen: U–Pb dating, Hf isotopes and trace elements in zircons from mantle xenoliths. *Journal of Petrology* **51**, 537–571. https://doi.org/10.1093/petrology/egp082.

Liu, X., Wang, W. R. Z., Zhao, Y., Liu, J. & Song, B. (2014). Early Neoproterozoic granulite facies metamorphism of mafic dykes from the Vestfold block, East Antarctica. *Journal of Metamorphic Geology* **32**, 1041–1062. https://doi.org/10.1111/jmg.12106.

Liu, P., Zhang, J., Massonne, H. J. & Jin, Z. (2018). Polyphase solid inclusions formed by interactions between infiltrating fluids and precursor minerals enclosed in garnet of UHP rocks from the Dabie Shan, China. *American Mineralogist* **103**, 1663–1673. https://doi.org/10.2138/am-2018-6395.

Liu, Z., Bartoli, O., Tong, L., Xu, Y. G. & Huang, X. (2020). Permian ultrahigh-temperature reworking in the southern Chinese Altai: evidence from petrology, P–T estimates, zircon and monazite U–Th–Pb geochronology. *Gondwana Research* **78**, 20–40. https://doi.org/10.1016/j.gr.2019.08.007.

Liu, X., Chen, L., Wang, W. R. Z., Zhao, Y., Ling, X. & Song, B. (2021). Deciphering early Neoproterozoic and Cambrian high-grade metamorphic events in the Archean/Mesoproterozoic Rauer group, East Antarctica. *Precambrian Research* **365**, 106392. https://doi.org/10.1016/j.precamres.2021.106392.

Lowenstern, J. B. (1995). Applications of silicate–melt inclusions to the study of magmatic volatiles. *Magmas, Fluids, and Ore Deposits* **23**, 71–99.

Ludwig, K. R. (1999) Using Isoplot/EX, Version 2. In: *A Geological Toolkit for Microsoft Excel*. California, Berkeley: Berkeley Geochronological Center, Special Publication 1a, p.47.

Luth, W. C., Jahns, R. H. & Tuttle, O. F. (1964). The granite system at pressure of 4 to 10 kilobars. *Journal of Geophysical Research* **69**, 759–773. https://doi.org/10.1029/JZ069i004p00759.

Morgan VI, G. B. & London, D. (2005). Effect of current density on the electron microprobe analysis of alkali aluminosilicate glasses. *American Mineralogist* **90**, 1131–1138. https://doi.org/10.2138/am.2005.1769.

Németh, P., Lehner, S. W., Petaev, M. I. & Buseck, P. R. (2013). Kumdykolite, a high-temperature feldspar from an enstatite chondrite. *American Mineralogist* **98**, 1070–1073. https://doi.org/10.2138/am.2013.4459.

O'Connor, J. T. (1965). A classification for quartz-rich igneous rocks based on feldspar ratios. *United States Geological Survey Professional Paper* **525**, 79–84.

Pan, J. Y., Ni, P. & Wang, R. C. (2019). Comparison of fluid processes in coexisting wolframite and quartz from a giant vein–type tungsten deposit, South China: insights from detailed petrography and LA–ICP–MS analysis of fluid inclusions. *American Mineralogist* **104**, 1092–1116. https://doi.org/10.2138/am-2019-6958.

Patiño Douce, A. E. & Johnston, A. D. (1991). Phase equilibria and melt productivity in the pelitic system: implications for the origin of peraluminous granitoids and aluminous granulites. *Contributions to Mineralogy and Petrology* **107**, 202–218. https://doi.org/10.1007/BF00310707.

Phillips, G., Wilson, C. J. L., Phillips, D. & Szczepanski, S. (2007). Thermochronological (Ar/Ar) evidence of early Palaeozoic basin inversion within the southern Prince Charles mountains, East Antarctica: implications for East Gondwana. *Journal of the Geological Society, London* **164**, 771–784. https://doi.org/10.1144/0016-76492006-073.

Pownall, J. M., Hall, R., Armstrong, R. A. & Forster, M. A. (2014). Earth's youngest-known ultrahigh-temperature granulites discovered on Seram, eastern Indonesia. *Geology* **42**, 279–282. https://doi.org/10.1130/G35230.1.

Redler, C., White, R. W. & Johnson, T. E. (2013). Migmatites in the Ivrea zone (NW Italy): constraints on partial melting and melt loss in metasedimentary rocks from Val Strona di Omegna. *Lithos* **175-176**, 40–53. https://doi.org/10.1016/j.lithos.2013.04.019.

Ren, L., Li, C., Wang, Y. & Liu, P. (2016). On constraining the Pan–African high–grade metamorphism time of the Larsemann Hills, East Antarctica. *Chinese Journal of Polar Research* **28**, 451–461 (in Chinese with English abstract).

Rosenberg, C. L. & Handy, M. R. (2005). Experimental deformation of partially melted granite revisited: implications for the continental crust. *Journal of Metamorphic Geology* **23**, 19–28. https://doi.org/10.1111/j.1525-1314.2005.00555.x.

Rudnick, R. L. & Gao, S. (2014) Composition of the continental crust. In: Rudnick R. L. (ed) *Treatise on Geochemistry*, 2nd edn. Elsevier Science Ltd., pp.1–51.

Rybach, L. (1988) Determination of heat production rate. In: Haenel R., Rybach L. & Stegena L. (eds) *Handbook of Terrestrial Heat–Flow Density Determination*. Dordrecht, Holland: Kluwer Academic Publishers, pp.125–142.

Santosh, M., Liu, S. J., Tsunogae, T. & Li, J. H. (2012). Paleoproterozoic ultrahigh-temperature granulites in the North China craton: implications for tectonic models on extreme crustal

metamorphism. *Precambrian Research* **222–223**, 77–106. https://doi.org/10.1016/j.precamres.2011.05.003.

Sawant, A. D., Gupta, S., Clark, C. & Misra, S. (2017) The Rauer–Rengali connection in the Indo–Antarctica amalgam: evidence from structure, metamorphism and geochronology. In: Pant N. C. & Dasgupta S. (eds) *Crustal Evolution of India and Antarctica: The Supercontinent Connection*. London: Geological Society, pp.171–196.

Sawyer, E. W., Cesare, B. & Brown, M. (2011). When the continental crust melts. *Elements* **7**, 229–234. https://doi.org/10.2113/gselements.7.4.229.

Scaillet, B., Holtz, F., Pichavant, M. & Schmidt, M. (1996). Viscosity of Himalayan leucogranites: implications for mechanisms of granitic magma ascent. *Journal of Geophysical Research: Solid Earth* **101**, 27691–27699. https://doi.org/10.1029/96JB01631.

Shabeer, K. P., Satish Kumar, M., Armstrong, R. & Buick, I. S. (2005). Constraints on the timing of Pan–African granulite–facies metamorphism in the Kerala Khondalite Belt of southern India: SHRIMP mineral ages and Nd isotopic systematics. *Journal of Geology* **113**, 95–106. https://doi.org/10.1086/425971.

Sims, J. R., Dirks, P. H. G. M., Carson, C. J. & Wilson, C. J. L. (1994). The structural evolution of the Rauer group, East Antarctica: mafic dykes as passive markers in a composite Proterozoic terrain. *Antarctic Science* **6**, 379–394. https://doi.org/10.1017/S0954102094000581.

Spreitzer, S. K., Walters, J. B., Cruz Uribe, A., Williams, M. L., Yates, M. G., Jercinovic, M. J., Grew, E. S. & Carson, C. J. (2021). Monazite petrochronology of polymetamorphic granulite–facies rocks of the Larsemann Hills, Prydz Bay, East Antarctica. *Journal of Metamorphic Geology* **39**, 1205–1228. https://doi.org/10.1111/jmg.12607.

Suzuki, K. & Kawakami, T. (2019). Metamorphic pressure–temperature conditions of the Lützow–holm complex of East Antarctica deduced from Zr–in–rutile geothermometer and Al_2SiO_5 minerals enclosed in garnet. *Journal of Mineralogical and Petrological Sciences* **114**, 267–279. https://doi.org/10.2465/jmps.190801.

Tacchetto, T., Bartoli, O., Cesare, B., Berkesi, M., Aradi, L. E., Dumond, G. & Szabó, C. (2019). Multiphase inclusions in peritectic garnet from granulites of the Athabasca granulite terrane (Canada): evidence of carbon recycling during Neoarchean crustal melting. *Chemical Geology* **508**, 197–209. https://doi.org/10.1016/j.chemgeo.2018.05.043.

Tacchetto, T., Reddy, S. M., Bartoli, O., Rickard, W. D. A., Fougerouse, D., Saxey, D. W., Quadir, Z. & Clark, C. (2021). Pre-nucleation geochemical heterogeneity within glassy anatectic inclusions and the role of water in glass preservation. *Contributions to Mineralogy and Petrology* **176**, 70. https://doi.org/10.1007/s00410-021-01826-0.

Taylor, R. J. M., Clark, C., Fitzsimons, I. C. W., Santosh, M., Hand, M., Evans, N. & McDonald, B. (2014). Post-peak, fluid mediated modification of granulite facies zircon and monazite in the Trivandrum block, southern India. *Contributions to Mineralogy and Petrology* **168**, 1–17. https://doi.org/10.1007/s00410-014-1044-0.

Tong, L. & Wilson, C. J. L. (2006). Tectonothermal evolution of the ultrahigh temperature metapelites from the Rauer group, East Antarctica. *Precambrian Research* **149**, 1–20. https://doi.org/10.1016/j.precamres.2006.04.004.

Tong, L., Xu, Y. G., Cawood, P. A., Zhou, X., Chen, Y. & Liu, Z. (2014a). Anticlockwise P–T evolution at ~280 ma recorded from ultrahigh-temperature metapelitic granulite in the Chinese Altai orogenic belt, a possible link with the Tarim mantle plume? *Journal of Asian Earth Sciences* **94**, 1–11. https://doi.org/10.1016/j.jseaes.2014.07.043.

Tong, L., Liu, X., Wang, Y. & Liang, X. (2014b). Metamorphic P–T paths of metapelitic granulites from the Larsemann Hills, East Antarctica. *Lithos* **192-195**, 102–115. https://doi.org/10.1016/j.lithos.2014.01.013.

Tong, L., Liu, Z., Li, Z. X., Liu, X. & Zhou, X. (2019). Poly-phase metamorphism of garnet–bearing mafic granulite from the Larsemann Hills, East Antarctica: P–T path, U–Pb ages and tectonic implications. *Precambrian Research* **326**, 385–398. https://doi.org/10.1016/j.precamres.2017.12.045.

Tong, L. X., Liu, Z. & Wang, Y. B. (2021). Research progress of the ultrahigh–temperature granulites in the Rauer group, East Antarctica. *Journal of Geomechanics* **27**, 705–718 (in Chinese with English abstract).

Wang, Y., Tong, L. & Liu, D. (2007) Zircon U–Pb ages from an ultra-high temperature metapelite, Rauer Group, east Antarctica: implications for overprints by Grenvillian and Pan–African events. In: Cooper A. K., Raymond C. R. *et al.* (eds) *A Keystone in a Changing World–Online Proceedings of the 10th ISAES. USGS Open–File Report 2007–1047, Short Research Paper 023, 4*. U.S. Geological Survey and The National Academies.

Wang, Y., Liu, D., Chung, S. L., Tong, L. & Ren, L. (2008). SHRIMP zircon age constraining from the Larsemann Hills region, Prydz Bay, for a late Mesoproterozoic to early Neoproterozoic tectono–thermal event in East Antarctica. *American Journal of Science* **308**, 573–617. https://doi.org/10.2475/04.2008.07.

Wang, X., Chou, M. I., Hu, W., Burruss, R. C., Sun, Q. & Song, Y. (2011). Raman spectroscopic measurements of CO_2 density: experimental calibration with high-pressure optical cell (HPOC) and fused silica capillary capsule (FSCC) with application to fluid inclusion observations. *Geochimica et Cosmochimica Acta* **75**, 4080–4093. https://doi.org/10.1016/j.gca.2011.04.028.

Wang, W. R. Z., Zhao, Y., Wei, C., Daczko, N. R., Liu, X., Xiao, W. & Zhang, Z. (2022). High-ultrahigh temperature metamorphism in the Larsemann Hills: insights into the Tectono–thermal evolution of the Prydz Bay region, East Antarctica. *Journal of Petrology* **63**, 1–30. https://doi.org/10.1093/petrology/egac002.

Warr, L. N. (2021). IMA–CNMNC approved mineral symbols. *Mineralogical Magazine* **85**, 291–320. https://doi.org/10.1180/mgm.2021.43.

Watt, G. R. & Harley, S. L. (1993). Accessory phase controls on the geochemistry of crustal melts and restites produced during water-undersaturated partial melting. *Contributions to Mineralogy and Petrology* **114**, 550–566. https://doi.org/10.1007/BF00321759.

Wei, C. J. (2016). Granulite facies metamorphism and petrogenesis of granite (II): quantitative modeling of the HT–UHT phase equilibria for metapelites and the petrogenesis of S-type granite. *Acta Petrologica Sinica* **32**, 1625–1643 (in Chinese with English abstract).

Weinberg, R. F. & Hasalová, P. (2015). Water–fluxed melting of the continental crust: a review. *Lithos* **212-215**, 158–188. https://doi.org/10.1016/j.lithos.2014.08.021.

Wheller, C. J. & Powell, R. (2014). A new thermodynamic model for sapphirine: calculated phase equilibria in K_2O–FeO–MgO–Al_2O_3–SiO_2–H_2O–TiO_2–Fe_2O_3. *Journal of Metamorphic Geology* **32**, 287–299. https://doi.org/10.1111/jmg.12067.

White, R. W., Powell, R. & Halpin, J. A. (2004). Spatially-focussed melt formation in aluminous metapelites from Broken Hill, Australia. *Journal of Metamorphic Geology* **22**, 825–845. https://doi.org/10.1111/j.1525-1314.2004.00553.x.

White, R. W., Stevens, G. & Johnson, T. E. (2011). Is the crucible reproducible? Reconciling melting experiments with thermodynamic calculations. *Elements* **7**, 241–246. https://doi.org/10.2113/gselements.7.4.241.

White, R. W., Powell, R., Holland, T. J. B., Johnson, T. E. & Green, E. C. R. (2014). New mineral activity–composition relations for thermodynamic calculations in metapelitic systems. *Journal of Metamorphic Geology* **32**, 261–286. https://doi.org/10.1111/jmg.12071.

Wilson, C. J. L., Quinn, C., Tong, L. & Philips, D. (2007). Early Palaeozoic intracratonic shears and post-tectonic cooling in the Rauer group, Prydz Bay, East Antarctica constrained by $^{40}Ar/^{39}Ar$ thermo–chronology. *Antarctic Science* **19**, 339–353. https://doi.org/10.1017/S0954102007000478.

Wolf, M., Romer, R. & Glodny, J. (2019). Isotope disequilibrium during partial melting of metasedimentary rocks. *Geochimica et Cosmochimica Acta* **257**, 163–183. https://doi.org/10.1016/j.gca.2019.05.008.

Zajacz, Z. & Halter, W. (2007). LA–ICPMS analyses of silicate melt inclusions in co-precipitated minerals: quantification, data analysis and mineral/melt partitioning. *Geochimica et Cosmochimica Acta* **71**, 1021–1040. https://doi.org/10.1016/j.gca.2006.11.001.

Zeng, L., Asimow, P. D. & Saleeby, J. B. (2005). Coupling of anatectic reactions and dissolution of accessory phases and the Sr and Nd isotope systematics of anatectic melts from a metasedimentary source. *Geochimica et Cosmochimica Acta* **69**, 3671–3682. https://doi.org/10.1016/j.gca.2005.02.035.

Zhang, X. Z., Wang, Q., Wyman, D., Kerr, A. C., Dan, W. & Qi, Y. (2022). Tibetan plateau insights into >1100° C crustal melting in the quaternary. *Geology* **50**, 1432–1437. https://doi.org/10.1130/G50387.1.

Zhao, Y., Liu, X., Song, B., Zhang, Z., Li, J., Yao, Y. & Wang, Y. (1995). Constraints on the stratigraphic age of the Larsemann Hills, East Antarctica: possible implications for Neo–Proterzoic tectonics. *Precambrian Research* **75**, 175–188. https://doi.org/10.1016/0301-9268(95)80005-3.

Zong, K. Q., Klemd, R., Yuan, Y., He, Z. Y., Guo, J. L., Shi, X. L., Liu, Y. S., Hu, Z. C. & Zhang, Z. M. (2017). The assembly of Rodinia: the correlation of early Neoproterozoic (ca. 900 ma) high-grade metamorphism and continental arc formation in the southern Beishan Orogen, southern central Asian Orogenic Belt (CAOB). *Precambrian Research* **290**, 32–48. https://doi.org/10.1016/j.precamres.2016.12.010.

Deltech Furnaces

Sustained operating temperatures to 1800° Celsius

www.deltechfurnaces.com

Gas Mixing System

An ISO 9001:2015 certified company

Custom Vertical Tube

ASME NQA-1 2008 Nuclear Quality Assurance

Standard Vertical Tube

Control systems are certified by Intertek UL508A compliant

Bottom Loading Vertical Tube